Journal of Drug Delivery Science and Technology 114 (2025) 107463

Contents lists available at ScienceDirect

Journal of Drug Delivery Science and Technology

journal homepage: www.elsevier.com/locate/jddst

Antimicrobial chitosan-silk fibroin scaffolds with green-synthesized metal oxide nanoparticles

Denisa-Maria Radulescu [a,c], Bodgan Stefan Vasile [b,c,d,*], Vasile-Adrian Surdu [e], Roxana-Doina Trusca [a], Cornelia-Ioana Ilie [a,c], Roxana Cristina Popescu [f,g], Ecaterina Andronescu [a,b,c], Veronica Drumea [h], Lia-Mara Ditu [i]

[a] Department of Science and Engineering of Oxide Materials and Nanomaterials, Faculty of Applied Chemistry and Materials Science, Faculty of Chemical Engineering and Biotechnologies, National University of Science and Technology POLITEHNICA Bucharest, 011061, Bucharest, Romania
[b] Romanian Academy of Scientists, 050045, Bucharest, Romania
[c] National Research Center for Micro and Nanomaterials, Faculty of Applied Chemistry and Materials Science, University Politehnica of Bucharest, 060042, Bucharest, Romania
[d] Research Center for Advanced Materials, Products and Processes, National University of Science and Technology POLITEHNICA Bucharest, 060042, Bucharest, Romania
[e] Department of Materials Science, Faculty of Materials Science and Engineering, Transilvania University of Brasov, 29 Eroilor Blvd., 500036, Brasov, Romania
[f] Department of Bioengineering and Biotechnology, Faculty of Medical Engineering, National University of Science and Technology POLITEHNICA Bucharest, 011061, Bucharest, Romania
[g] Department of Life and Environmental Physics, National Institute for R&D in Physics and Nuclear Engineering "Horia Hulubei", 077125, Magurele, Romania
[h] S.C. BIOTEHNOS S.A., Gorunului 3-5, 075100, Otopeni, Romania
[i] Department of Botany and Microbiology, Faculty of Biology, University of Bucharest, 060101, Bucharest, Romania

A B S T R A C T

In recent years, soft tissue injuries caused by trauma or pathological diseases have represented a major problem regarding patient treatment and recovery. Traditional wound dressings often lack the necessary biological activity or maintain a moist environment, therefore reducing their efficiency. To solve this problem, this study focused on the development of multifunctional silk fibroin-chitosan composite scaffolds that contain green-synthesized metal oxide nanoparticles (NPs) for wound healing applications. Zinc oxide, copper oxide, and magnesium oxide NPs were synthesized using orange peel extract as a reducing and capping agent in their green synthesis process. The scaffolds were created with different CS/SF ratios (1:1 and 2:1) and NP concentrations (0.05 %, 0.1 %, and 0.15 % w/w). For the characterization of the biomaterials, X-ray diffraction, scanning electron microscopy, and Fourier-transform infrared spectroscopy were performed to evaluate the morphological and chemical features of the obtained scaffolds. Furthermore, swelling behavior and antibacterial activity have also been evaluated to determine if the obtained scaffolds could act as ideal materials for wound healing applications. The results showed that NP addition increased the swelling capability and the antibacterial activity against *Staphylococcus aureus* and methicillin-resistant *Staphylococcus aureus 44* (MRSA) of the biomaterials. Moreover, the 1:1 CS/SF scaffolds displayed higher water absorption and antibacterial capacities than those with a 2:1 ratio. Therefore, our research demonstrated that the created SF/CS scaffolds that contained green-synthesized NP provide a promising dressing for wound healing by offering increased biocompatibility, biodegradability, and antibacterial activity.

Abbreviation	Full Term
MRSA	Methicillin-Resistant *Staphylococcus aureus*
CS	Chitosan
SF	Silk Fibroin
NP	Nanoparticle
NPs	Nanoparticles
ZnO	Zinc Oxide
CuO	Copper Oxide
MgO	Magnesium Oxide
XRD	X-ray Diffraction
SEM	Scanning Electron Microscopy
FTIR	Fourier-Transform Infrared Spectroscopy
ECM	Extracellular Matrix
CFU	Colony-Forming Unit

(*continued on next column*)

(*continued*)

(*continued on next page*)

* Corresponding author. Romanian Academy of Scientists, 050045, Bucharest, Romania.
E-mail addresses: denisa.m.radulescu@gmail.com (D.-M. Radulescu), bogdan.vasile@upb.ro (B.S. Vasile), adrian.surdu@upb.ro (V.-A. Surdu), roxana_doina.trusca@upb.ro (R.-D. Trusca), cornelia_ioana.ilie@upb.ro (C.-I. Ilie), Roxana.popescu1108@upb.ro (R.C. Popescu), veronica.drumea@biotehnos.com (V. Drumea), lia-mara.ditu@bio.unibuc.ro (L.-M. Ditu).

https://doi.org/10.1016/j.jddst.2025.107463
Received 12 April 2025; Received in revised form 18 August 2025; Accepted 27 August 2025
Available online 28 August 2025

(*continued*)

Abbreviation	Full Term
PBS	Phosphate-Buffered Saline
EDX or EDS	Energy-Dispersive X-ray Spectroscopy
ANOVA	Analysis of Variance
CLSI	Clinical and Laboratory Standards Institute
SD	Swelling Degree
ROS	Reactive Oxygen Species
LDH	Lactate Dehydrogenase

1. Introduction

Over the years, wound healing, especially in chronic and infected wounds, has remained a major therapeutic problem. In this direction, traditional dressings, such as gauze and bandages, while extensively used, frequently fail to maintain the moist environment required for optimum healing and lack natural antibacterial characteristics [1–5]. As a result, there is an increasing demand for bioactive wound dressings that offer structural support, moisture retention, and antibacterial properties [6]. Thus, bioengineered scaffolds have emerged as viable alternatives to conventional dressings due to their ability to mimic the extracellular matrix (ECM) and promote tissue regeneration [7–9]. An ideal scaffold must be biocompatible, biodegradable, antibacterial, and capable of maintaining a moist environment that promotes cell proliferation and migration [9]. In the group of materials selected for such scaffolds, silk fibroin (SF) and chitosan (CS) are distinguished due to their particular structural and biological features [10–14].

Related to SF, the polymer exhibits great mechanical strength and structural mimicry of the ECM, although it lacks antibacterial properties. On the other hand, CS has antibacterial and hemostatic characteristics while having mechanical limits [15–18]. As a result, CS/SF composite scaffolds provide a balanced approach by using the characteristics of both biopolymers. However, even when combined, their antibacterial effectiveness is insufficient for treatment in acute or chronic wounds. Metal oxide nanoparticles (NPs) such as ZnO, CuO, and MgO have gained growing popularity for improving scaffold functionality due to their powerful and broad-spectrum antibacterial properties, low cytotoxicity, and capacity to stimulate wound healing [19–25]. However, conventional NP production frequently requires hazardous chemicals, limiting biomedical relevance. Green synthesis employing plant extracts offers a safer, more sustainable method, eliminating toxic chemicals and increasing NP biocompatibility [26–28].

Although various studies have studied the introduction of specific metal oxide NPs—particularly ZnO or CuO—into SF- or CS-based scaffolds, most of these studies have relied on chemically produced NPs and focused on only one type of NP [29]. While many studies have examined the integration of ZnO NPs into SF scaffolds, the development of SF composite porous scaffolds is still limited, particularly in wound healing applications [30]. These scaffolds may enable the incorporation of various metal oxide NPs for in vivo and in vitro evaluations. In addition, despite MgO and CuO NPs' superior antibacterial, anti-inflammatory, and antioxidant characteristics, research into their incorporation into SF scaffolds is limited [31]. Hence, additional research is needed to determine the biological effects of these NPs, particularly when green synthesis methods are used, as this technology has the potential to reduce waste and pollution and use safer solvents. By embedding these green-synthesized metal oxide NPs within scaffolds, innovative composite materials that might have wound-healing applications could be designed [32]. Moreover, modern studies on SF scaffolds for tissue engineering applications have mainly ignored the use of metal oxide NPs such as CuO, ZnO, and MgO, instead focusing on FeO or graphene oxide NPs [30]. Metal oxide NPs are crucial for SF scaffolds because they can increase antibacterial efficiency while producing low toxicity. Furthermore, combining CuO/ZnO/MgO NPs with natural polymers like chitosan may enhance the scaffold's biological and antibacterial activities, making them excellent biomaterials for tissue engineering and wound healing [33].

These methods offer limited knowledge into the potential synergistic interactions of metal oxides. By contrast, this study is the first to combine green-synthesized ZnO, CuO, and MgO NPs into CS/SF composite scaffolds. The green fabrication technique should improve NP biocompatibility while lowering environmental and cytotoxic concerns. This innovative, multipurpose scaffold platform thereby addresses critical limitations of earlier single-NP designs and represents a considerable breakthrough in chronic wound dressing materials. In addition, this research focuses on the development and evaluation of CS/SF composite scaffolds incorporated with green-synthesized ZnO, CuO, and MgO NPs for wound healing applications. The scaffolds obtained have been evaluated to assess their structure, morphology, and chemical properties, but also their swelling behavior. Additionally, antimicrobial activity has been assessed against selected pathogens such as *Staphylococcus aureus* and MRSA methicillin-resistant *S. aureus* (MRSA) and *S. epidermidis* to obtain biocompatible, biodegradable scaffolds as a sustainable alternative to traditional wound dressings.

2. Materials and methods

2.1. Materials

For the synthesis of ZnO, CuO, and MgO NPs, zinc nitrate hexahydrate (Sigma-Aldrich, 98 %), cupric nitrate hemi(pentahydrate) (Sigma-Aldrich, 98 %), and magnesium nitrate hexahydrate (Honeywell, Fluka, 98 %), have been used. To prepare the orange peel extract, 2 kg of oranges were purchased from the local market. For the development of SF/CS scaffolds, SF was obtained from AliExpress (Zhejiang, China), while CS (high molecular weight, 310,000–375,000 Da) was acquired from Sigma-Aldrich (Germany, Darmstadt), and acetic acid from Sigma-Aldrich (Germany, Darmstadt). The microbiological activity was performed using Nutrient Broth No. 2 and agar purchased from Sigma-Aldrich (Germany, Darmstadt). All strains tested in this study are provided by the Microorganisms Collection of the Department of Microbiology, Faculty of Biology & Research Institute of the University of Bucharest. For the cytotoxicity evaluation, immortalized murine fibroblast L929 cells (ATCC, Manassas, VA, USA) and primary human dermal fibroblast BJ cells (ATCC, Manassas, VA, USA) were cultured in Dulbecco's Modified Eagle Medium (DMEM), supplemented with 10 % fetal bovine serum and 1 % Penicillin-Streptomycin, under standard temperature and humidity conditions (37 °C, 5 % CO_2, 90 % humidity).

2.2. Synthesis of nanoparticles

In this green synthesis approach, *Citrus sinensis* peel extract has been obtained by washing and peeling the oranges. The peels were dried in an oven at 40 °C for 4 h, then ground into a fine powder using a mortar for 30 min. Furthermore, a 2 % orange peel powder solution was mixed with distilled water and stirred magnetically for 1 h, followed by ultrasonic treatment at 60 °C for 1 h. After maceration, the mixture was filtered, and the resulting extract was stored in a refrigerator for later use in synthesizing all types of NPs. For the green synthesis of CuO and ZnO NPs, the procedure was similar, with adjustments only in the metal precursors. The metal salt was combined with the orange extract for 1 h and then treated in an ultrasound bath at 60 °C for another hour. The resulting NPs were dried in an oven at 150 °C. Specifically, for CuO NPs, 4.70 % cupric nitrate was added to the extract, and after mixing, the solution was dried at 60 °C and then calcined at 300 °C for 2 h, with a heating rate of 5 °C/min. For ZnO NPs, 5.87 % zinc nitrate was used, following the same steps, but with a final calcination at 400 °C for 2 h under the same heating rate. The synthesis of MgO NPs involved preparing two solutions simultaneously: one with orange extract and the other with a 5 % metal salt solution. The orange extract was added

Table 1
CS/SF composite scaffolds and sample labels.

Sample	Chitosan/Silk Fibroin (v/v)	ZnO NPs (% w/w)	CuO NPs (% w/w)	MgO NPs (% w/w)
CS/SF 1-1	1:1	–	–	–
CS/SF 2-1	2:1	–	–	–
CS/SF 1-1 ZnO 0.05	1:1	0.05	–	–
CS/SF 2-1 ZnO 0.05	2:1	0.05	–	–
CS/SF 1-1 ZnO 0.1	1:1	0.10	–	–
CS/SF 2-1 ZnO 0.1	2:1	0.10	–	–
CS/SF 1-1 ZnO 0.15	1:1	0.15	–	–
CS/SF 2-1 ZnO 0.15	2:1	0.15	–	–
CS/SF 1-1 MgO 0.05	1:1	–	–	0.05
CS/SF 2-1 MgO 0.05	2:1	–	–	0.05
CS/SF 1-1 MgO 0.1	1:1	–	–	0.10
CS/SF 2-1 MgO 0.1	2:1	–	–	0.10
CS/SF 1-1 MgO 0.15	1:1	–	–	0.15
CS/SF 2-1 MgO 0.15	2:1	–	–	0.15
CS/SF 1-1 CuO 0.05	1:1	–	0.05	–
CS/SF 2-1 CuO 0.05	2:1	–	0.05	–
CS/SF 1-1 CuO 0.1	1:1	–	0.10	–
CS/SF 2-1 CuO 0.1	2:1	–	0.10	–
CS/SF 1-1 CuO 0.15	1:1	–	0.15	–
CS/SF 2-1 CuO 0.15	2:1	–	0.15	–

dropwise to the metal salt solution, and the pH was adjusted to 12 using ammonia (25 % NH_3). Once the desired pH was reached, the mixture was stirred for 4 h, then filtered, dried at 150 °C, and finally calcined at 400 °C for 2 h, also at a 5 °C/min heating rate.

2.3. Synthesis of nanoparticles silk fibroin/chitosan composite scaffolds

To achieve a homogeneous 2 % (w/v) SF solution, the polymer was dissolved in distilled water with continuous magnetic stirring for approximately 30 min. Simultaneously, CS was dissolved in a 2 % (v/v) acetic acid solution using magnetic stirring until fully dissolved, obtaining a 2 % (w/v) CS solution. The base polymer matrix was formed by mixing the SF and CS solutions in two volumetric ratios, 1:1 and 2:1 (CS:SF, v/v). For nanoparticle-incorporated scaffolds, green-synthesized ZnO, CuO, or MgO NPs were introduced to the SF solution before blending at concentrations of 0.05 %, 0.1 %, or 0.15 % (w/w relative to the total polymer weight), as stated in Table 1. The nanoparticle-containing SF solution was stirred thoroughly to ensure uniform dispersion before combining with the CS solution. After mixing, the resulting blends were cast into molds and frozen at −20 °C for 12 h to stabilize the scaffold structure. The frozen samples were then subjected to lyophilization at −80 °C for 72 h to remove water and create a porous three-dimensional scaffold network. The obtained scaffolds exhibited a highly porous architecture, as confirmed by SEM analysis, making them suitable for wound healing applications.

2.4. X-ray diffraction analysis

Room temperature X-ray diffraction measurements were performed to investigate the phase composition and crystallinity. For this purpose, a Bruker D8 Advance diffractometer using Ni-filtered Cu-Kα radiation (λ = 1.5418 Å) was used. The X-ray tube was operated at 40 kV and 40 mA. On the incident beam side motorized slits with 0.25 mm opening and a 2.5° soller slit were used and on the diffracted beam side motorized slits with 5 mm opening and Ni 0.02 were mounted on LYNXEYE XE-T detector operated in 1D mode and high resolution option. The X-ray diffraction patterns were recorded in the 20–80° 2θ range, with a step size of 0.02° and a counting time of 0.2 s/step. Data reduction and search-and-match methods were carried out using HighScorePlus software version 3.0.e and the Crystallography Open Database database.

2.5. Scanning electron microscopy analysis

Scanning Electron Microscopy (SEM) has been used to examine the size and shape of the green-manufactured NPs. Images have been captured using a Quanta Inspect F50 scanning electron microscope from FEI Company (Eindhoven, Netherlands), which includes a field emission gun electron source (FEG) with a resolution of 1.2 nm and an energy dispersive X-ray spectrometer with a MnK resolution of 133 eV. The size of the green-synthesized NPs has been determined by examining SEM micrographs with ImageJ software (National Institutes of Health, USA). To establish statistical relevance, for each sample, around 100 unique nanoparticles have been measured and analyzed. Particle diameters were measured manually, and the results were utilized to create size distribution histograms, which allowed the mean size and standard deviation to be calculated. Although SEM pictures (Figs. 2–4) showed some degree of nanoparticle aggregation, only clearly discernible individual particles were chosen for measurement to prevent skewing the results. To maintain accuracy and consistency, aggregate clusters were removed from the size analysis.

2.6. Fourier-transform infrared (FTIR) spectroscopy analysis

The functional groups found in the NPs were identified with a Nicolet iS50 FTIR spectrometer (Nicolet, MA, USA). This device features a DTGS detector with high sensitivity from 4000 cm^{-1} to 400 cm^{-1} and a resolution of 4 cm^{-1}, obtained by averaging 32 scans to enhance spectral quality. The measurements were taken at room temperature, and the data was recorded and analyzed using Omnic32 software.

2.7. GC-MS analysis

The study was carried out utilizing a Thermo Scientific TRACE 1310 gas chromatograph and a TSQ-8000EV0 triple quadrupole mass spectrometer with a TriPlus RSH autosampler. The separation was performed on a ZB-5MS Zebron capillary column (30 m × 0.25 mm × 0.25 μm) using ultra-high purity helium (99.999 %) as the carrier gas at a constant flow rate of 1.0 mL/min. The mass spectrometer functioned in electron ionization (EI) mode at 70 eV, with a scan range of 40–650 *m/z* and a scan period of 0.2 s. The injector temperature was set at 280 °C, and samples were introduced using a 1 μL injection (10:1 split ratio). The GC oven temperature program started at 60 °C (which took place for 1 min), ascended at 10 °C/min to 190 °C, and then ascended at 15 °C/min to 300 °C (held for 30 min). The transfer line and ion source temperatures were kept at 280 °C and 230 °C, respectively.

The orange peel extract (72 mL) was thoroughly extracted with hexane (2 × 35 mL). The organic phases were then dried over anhydrous Na_2SO_4 and concentrated to ~1 mL using a rotary evaporator (Büchi R-300 at 40 °C and 300 mbar). The remaining solvent was removed using a moderate nitrogen stream, and the dry extract was reconstituted in 1 mL of HPLC-grade ethyl acetate for GC-MS analysis. To analyze polar constituents, the aqueous phase (0.5 mL) was evaporated under nitrogen

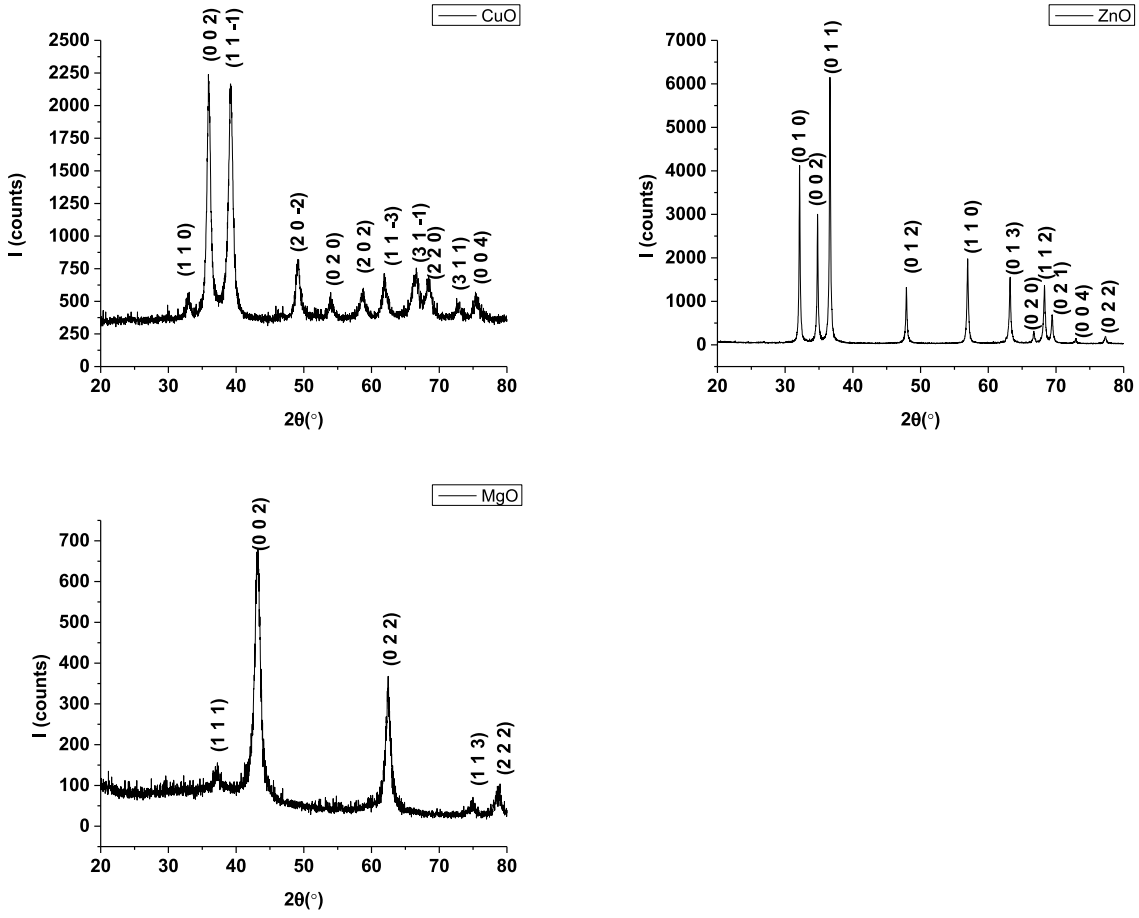

Fig. 1. X-ray diffractogram for green synthesized CuO, ZnO, and MgO NPs.

and derivatized with 100 μL of BSTFA (containing 1 % TMCS) at 70 °C for 30 min. Chromeleon software was used to acquire and process data. Compounds were identified by comparing mass spectra to the NIST database [34] and, where appropriate, verified with retention indices. Major chemicals (such as terpenoids and methoxyflavones) were quantified using peak regions from the total ion chromatogram.

2.8. Swelling rate

The lyophilized scaffolds were shaped into cylinders with a diameter of 5 mm to assess their swelling capacity. Each sample was immersed in phosphate-buffered saline (PBS, ROTI®Fair PBS 7.4, Dautphetal, Germany) to create a solution that mimics the ion content of body plasma. The swelling ratio was calculated using the following equation:

$$Swelling\ ratio\ (\%) = \frac{Wt - Wi}{W_i} \times 100\% \quad (1)$$

where W_i is the initial mass of the sample (before immersion in PBS), and W_t is the mass of the sample measured at various time points after immersion and weighing.

2.9. Antimicrobial activity evaluation

The anti-adherent capacity of the CS/SF-based scaffolds developed in this research was determined by the colony-forming units/mL values (CFU/mL) [35–37]. Antibacterial activity has been assessed against *Staphylococcus aureus* ATCC 25923, methicillin-resistant *Staphylococcus aureus 44* (MRSA 44, a clinical isolate from cutaneous wounds), and *Staphylococcus epidermidis* (clinical isolate). Contaminants did not affect the experiment because all samples had been previously sterilized and exposed to UV light for 30 min on each side. Furthermore, UV radiation activates the NPs found in the membrane structure.

Bacterial cell suspensions (1.5×10^8 CFU/mL) have been prepared in a sterile physiological buffer (PBS) from fresh cultures (18–24 h). The quantitative evaluation of the antibacterial activity of each sample was performed using a Nutrient broth: bacterial cell suspension ratio = 10:1, and the final density of 1.5×10^7 CFU/mL. Scaffold anti-adherence was tested as described previously [35–37], while biofilm formation was quantified following the CLSI standard [38]. The viable colony formation was measured in CFU (colony-forming units)/mL. The CFU/mL values were expressed as the mean of the total number of colonies × 1/D (where D is the decimal dilution used to estimate the total number of colonies) [35–37]. The assays were carried out in three different experiments.

2.10. Cytotoxicity evaluation

To evaluate the cytotoxicity of the developed scaffolds, L929 mouse fibroblasts (ATCC, Virginia, MA, USA) were cultured in Dulbecco's Modified Eagle Medium (DMEM), supplemented with 10 % fetal bovine serum and 1 % Penicilin-Streptomicyn, in standard conditions of temperature and humidity (37°C, 5 % CO_2, 90 % humidity).

The cells were seeded at a concentration of 100,000 cells/mL/well in a 12-well plate and incubated under standard temperature and humidity conditions for 24 h to allow adhesion. After incubation, a sponge sample was placed on each cell monolayer, and the plates were incubated under standard temperature and humidity conditions in the presence of nanoparticles for 7 days, respectively. Following this, cell viability

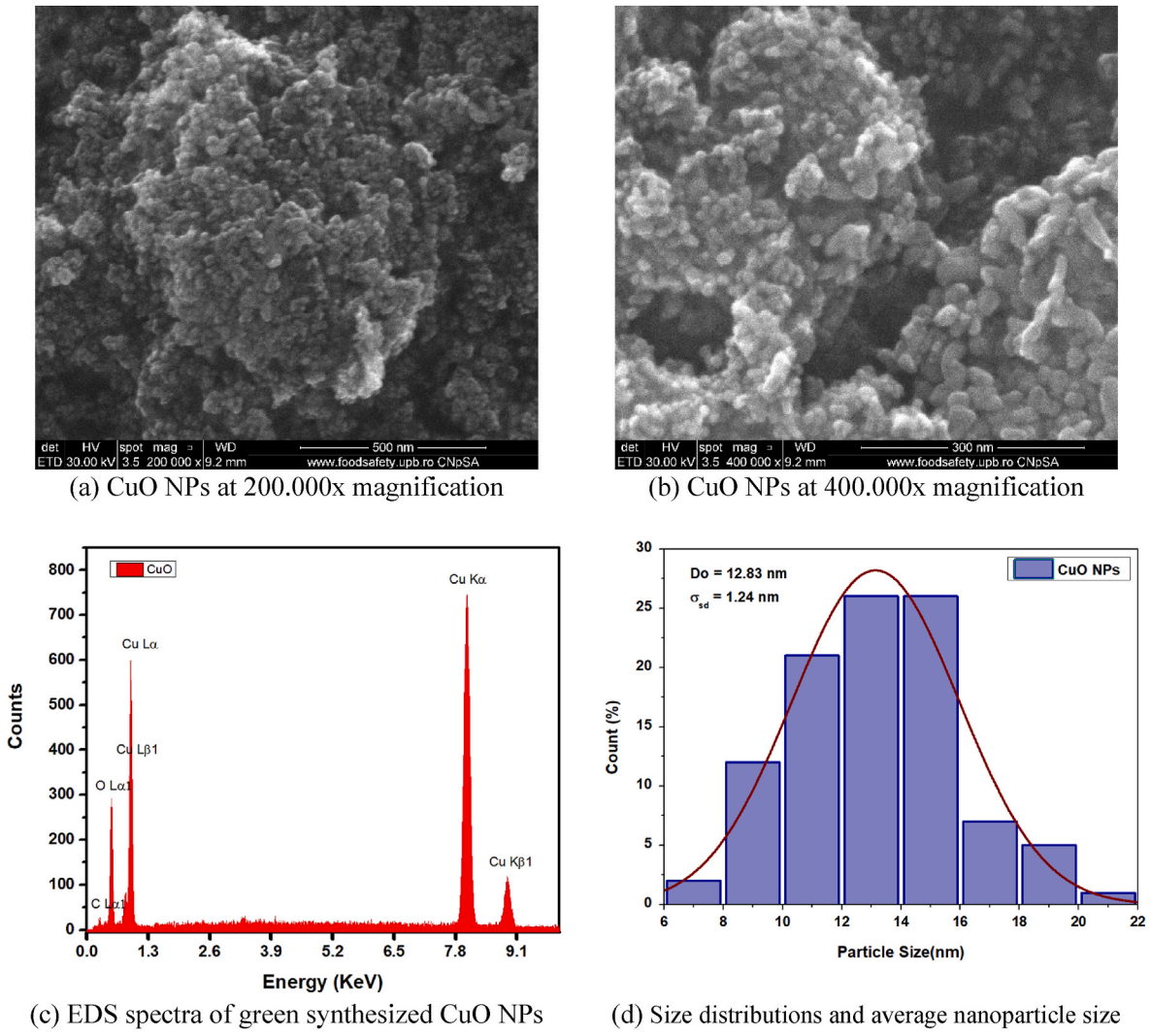

Fig. 2. SEM micrographs obtained for green-synthesized CuO NPs. (For interpretation of the references to colour in this figure legend, the reader is referred to the Web version of this article.)

assays were performed. Data were expressed as mean ± standard deviation (STDEV), and statistical evaluation was performed using Student's t-test, with significance levels set at *p < 0.05, **p < 0.01, and ***p < 0.001. Cell morphology was evaluated without prior sample preparation.

2.10.1. Lactate Dehydrogenase (LDH) release

After the incubation period, 50 μL of supernatant from each well was collected and transferred to a new 96-well plate to measure the amount of LDH released by the cells due to interaction with the biomaterial. LDH is a cytosolic enzyme that acts as a catalyst in the metabolic conversion of lactate to pyruvate. LDH is released into the extracellular medium only due to cell membrane damage, making extracellular LDH a marker of necrotic cell death. To quantify LDH release following exposure of human osteoblasts to ceramic biomaterials, the CyQUANT LDH Cytotoxicity Assay (Invitrogen, Thermo Fisher Scientific, Waltham, Massachusetts, USA) was used. The samples were prepared according to the manufacturer's instructions (by incubation with a series of reagents), and absorbance was measured at 490 nm. The amount of LDH released was calculated relative to the negative control (assigned a value of 1), which consisted of cells not exposed to the biomaterial. The negative control was represented by cells incubated only with complete culture medium.

2.11. Statistical analysis

The data results were analyzed using GraphPad Prism 10 by GraphPad Software, San Diego, California (USA). We compared the differences between groups using analysis of variance (ANOVA) and Tukey's/Holm-Šídák's multiple comparisons test. The differences between samples were considered statistically significant when the *p*-value was <0.05.

3. Results

3.1. X-ray diffraction (XRD) analysis

The crystalline phase composition of all green-synthesized powders was studied by XRD analysis, and the findings are shown in Fig. 1. The XRD patterns for CuO, ZnO, and MgO NPs demonstrate high crystallinity, as evidenced by sharp and well-defined peaks. Thus, the X-ray diffraction pattern of the CuO powder obtained after calcination at 300 °C shows a single-phase composition indexed with the tenorite CuO phase (COD # 96-901-6056) with monoclinic symmetry and specific peaks associated with the Miller indices (110), (002), (11-1), (20-2), (020), (202), (11-3), (31-1), (220), (311) and (004). The crystallite size measured by whole pattern Rietveld refinement showed an average size of 8.91 ± 0.68 nm.

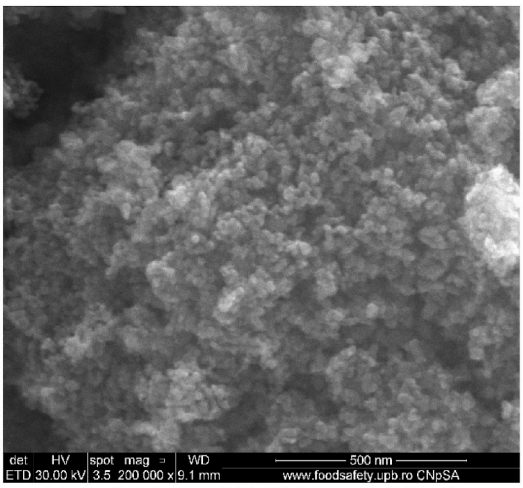

(a) ZnO NPs at 200.000x magnification

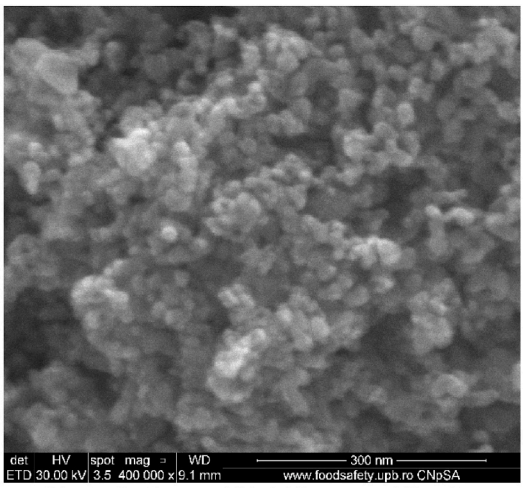

(b) ZnO NPs at 400.000x magnification

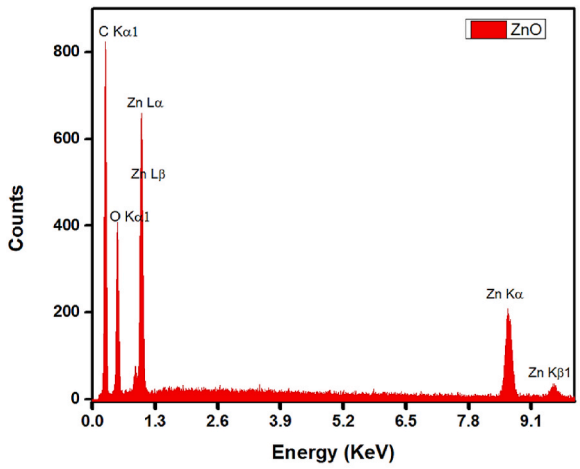

(c) EDS spectra of green synthesized CuO NPs

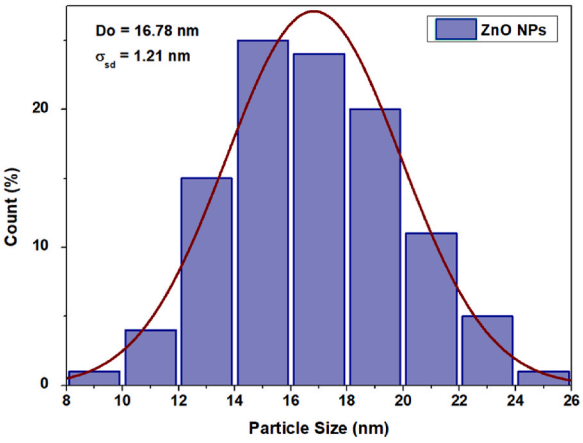

(d) Size distributions and average nanoparticle size

Fig. 3. SEM micrographs obtained for green synthesized ZnO NPs. (For interpretation of the references to colour in this figure legend, the reader is referred to the Web version of this article.)

ZnO NPs obtained after thermal treatment at 400 °C resulted in the successful generation of NPs with hexagonal crystal symmetry, as proven by the COD # 96-900-8878 file. The diffraction pattern showed distinct peaks which corresponded to the Miller indices (010), (002), (011), (012), (110), (013), (020), (112), (021), (004), and (022). Furthermore, the analysis revealed that the ZnO NPs have an average crystallite size of 34.01 ± 7.03 nm. Similarly, after calcination at 300 °C, the MgO powder was successfully transformed into MgO NPs, as confirmed by the COD #96-900-0495 file. The NPs exhibited cubic symmetry, with specific peaks corresponding to the Miller indices (111), (002), (022), (113), and (222), respectively. Further, the obtained NPs had an average crystallite size of 6.99 ± 0.25 nm.

3.2. Scanning electron microscopy (SEM) analysis

3.2.1. Morphological characterization of green synthesized metal oxide nanoparticles

Figs. 2–4 show SEM images of the obtained NPs, which provide information about their morphology and structural features. A careful evaluation of each sample reveals individual properties while also showing common features among the many nanoparticle categories. As a result, the CuO NPs, as shown in Fig. 2, display a granular morphology and a strong tendency to agglomerate. This clustering characteristic can be mainly attributed to the NPs' large surface area, which results in enhanced surface energy, and the consequence of small dimensions NPs, ranging from 3 to 20 nm. The elemental composition of the bio-synthesized CuO NPs was validated by EDX analysis, and the corresponding spectra are shown in Fig. 2c [39]. Carbon atoms detected in the EDX spectrum may appear from multiple sources, including the conductive carbon tape used for EDX sample preparation, remaining organic compounds from the plant extract adhering to the CuO NPs surface, and unforeseen carbon contamination, which is commonly found in samples exposed to ambient conditions [40]. Furthermore, the quantitative assessment using histogram evaluation (Fig. 2d) revealed a mean particle size of 12.83 ± 1.24 nm, with the majority of particles concentrated between 10 and 16 nm range.

In a similar pattern, the ZnO NPs displayed in Fig. 3 exhibit several similar morphological characteristics to CuO NPs. These particles also have granular morphology and show strong agglomeration tendencies. The size distribution study in Fig. 3d shows that the ZnO NPs have a mean particle size of 16.78 ± 1.21 nm, a bit larger than the CuO NPs. The particle sizes predominantly range between 8 and 26 nm, with most particles concentrated in the 14–20 nm interval. This narrow size range reflects effective control over the particle growth during the synthesis process, resulting in a uniform morphology with minimal size variation. In addition, Fig. 3c also presents the elemental composition of the bio-synthesized ZnO NPs, validated by EDX analysis, and the corresponding spectra.

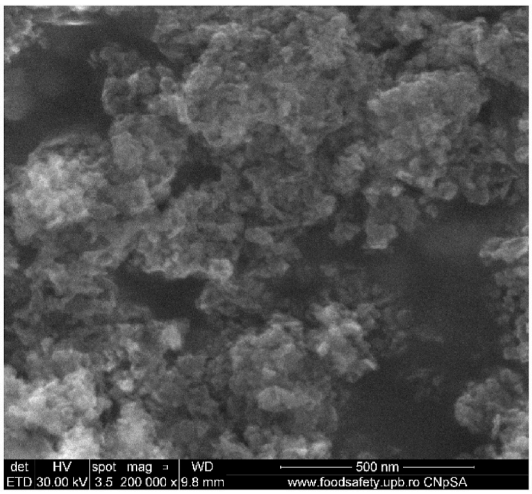

(a) MgO NPs at 200.000x magnification

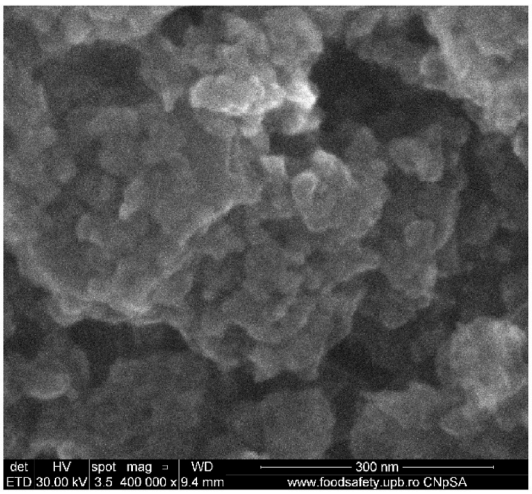

(b) MgO NPs at 400.000x magnification

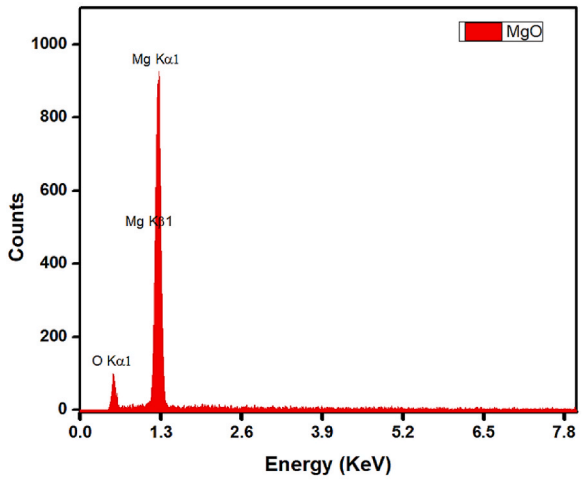

(c) EDS spectra of green synthesized MgO NPs

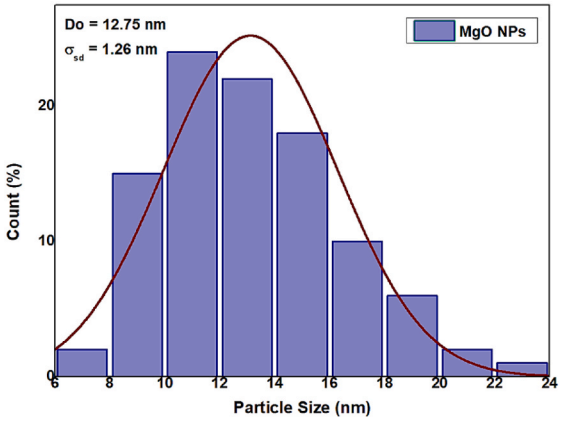

(d) Size distributions and average nanoparticle

Fig. 4. SEM micrographs obtained for green-synthesized MgO NPs.

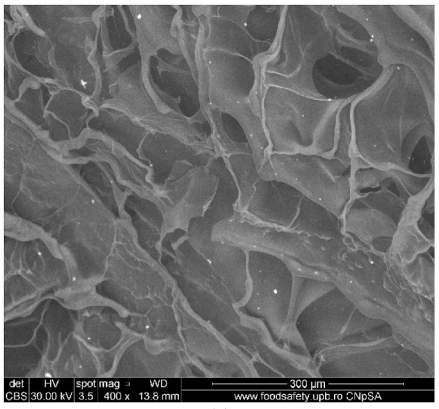

(a)

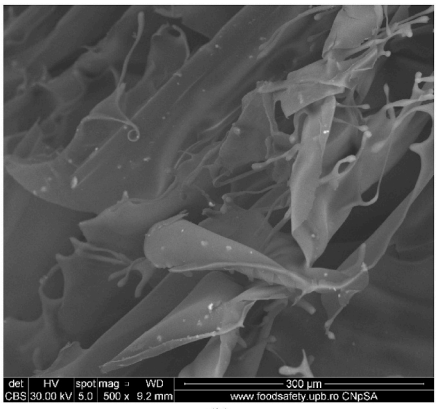

(b)

Fig. 5. SEM micrographs (scale bar: 300 µm) of 1-1 CS/SF scaffolds incorporating (a) green synthesized 0.05 % CuO NPs observed at x400 magnification and (b) green synthesized 0.05 % ZnO observed at x500 magnification.

However, MgO NPs exhibit distinct features when compared to CuO and ZnO samples. As seen in Fig. 4, these NPs have an irregular morphology and a significantly higher level of aggregation. Furthermore, Fig. 4c displays the EDX spectra, confirming the elemental composition of the biologically synthesized MgO nanoparticles. Although their size ranges from 10 to 40 nm, the histogram analysis (Fig. 4d) shows a mean particle size of 12.75 ± 1.26 nm, which is similar to that of CuO NPs despite their irregular form. The particle sizes

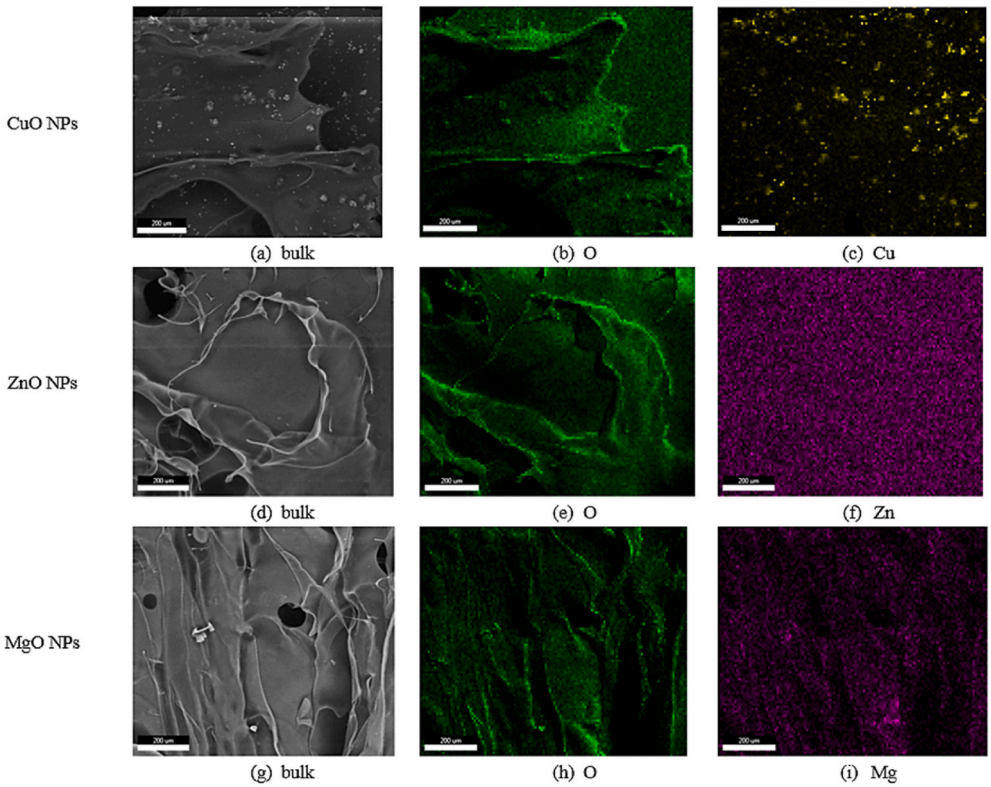

Fig. 6. Elemental mappings of CS/SF 1-1 CuO 0.1 % composite scaffolds (a–c), CS/SF 1-1 ZnO 0.1 % composite scaffolds(d-f), and CS/SF 1-1 MgO 0.1 % composite scaffolds (g–i), respectively. All samples have a scale bar: 200 μm.

predominantly range between 6 and 24 nm, with most particles concentrated in the 10–24 nm interval. The observed agglomeration across all three NP types can thus be attributed to fundamental physicochemical principles: their high surface area-to-volume ratio leads to increased surface energy, whereas their nanoscale dimensions enhance van der Waals forces, collectively promoting particle clustering [41,42]. This behavior, while particularly noticeable in the MgO sample, is a common feature of all produced NPs.

3.2.2. *Morphological characterization of CS/SF composite scaffolds*

Figs. S1–S4 show SEM micrographs of CS/SF scaffolds containing green-synthesized ZnO, MgO, and CuO NPs at varying concentrations (0.05 %, 0.1 %, and 0.15 %), seen at × 500 magnification. Additionally, by checking Fig. 5, a clear example of the NPs integration within the scaffolds can also be observed. These micrographs provide important insights into how nanoparticle integration affects the scaffold structure. As a result of evaluating the obtained micrographs, it was found that the produced scaffolds have a highly porous design, which is important for wound healing applications. Numerous prior investigations have demonstrated that the porosity generated by the scaffold architecture is critical for cell growth, nutrient transport, and waste elimination. Furthermore, it has been noticed that the addition of ZnO, MgO, and CuO NPs does not alter the overall porous structure. However, when the concentration of NPs increases, significant changes in pore size uniformity and distribution occur. Moreover, it was concluded that the NPs are dispersed throughout the scaffold matrix, although their behavior varies according to type and concentration. At higher concentrations, particularly 0.15 %, aggregation is highlighted, resulting in localized densification and potential modifications in the mechanical properties of the scaffolds.

Furthermore, regardless of the kind of metal oxide, ZnO, MgO, and CuO NPs exhibit similar overall integration behavior into the CS/SF scaffold matrix, despite their distinct crystalline structures and chemical compositions. This constant integration behavior across all NP types implies that the size of the nanoparticles and the scaffold-development technique, rather than the particular metal oxide chemistry, are the primary determinants of the physical incorporation mechanism. The basic integration behavior into the scaffold matrix is not significantly impacted by the kind of NPs, suggesting that the lyophilization-based scaffold manufacturing approach offers a stable platform for integrating different metal oxide nanoparticles while preserving structural integrity.

Fig. 6 present the elemental mapping of CS/SF 1-1 composite scaffolds that contain 0.1 % CuO, ZnO, and MgO NPs. Fig. 6a–c displays the distribution of oxygen and copper, revealing the most pronounced heterogeneity distribution of CuO among all three types of metal oxide NPs. This heterogeneity may be attributed to the small NPs dimension (between 3 and 20 nm), suggesting significant agglomeration of nanoparticles. The smaller dimensions are likely to contribute to higher surface energy, intensify van der Waals forces and surface energy effects, resulting in stronger agglomeration tendencies as noted in the morphological analysis, and therefore promote clustering during scaffold formation.

Fig. 6d–f presents the distribution of oxygen and zinc, indicating that ZnO is more uniformly integrated into the scaffold compared to CuO and MgO. This increased homogeneous distribution is associated with ZnO's bigger NP dimensions, which may result in smaller tendencies of agglomeration. The well-distributed ZnO NPs might enhance structural stability and tissue regeneration efficiency by facilitating uniform mechanical and biological interactions across the scaffold matrix. Fig. 6g–i illustrates the distribution of oxygen and magnesium, demonstrating that MgO NPs exhibit a partially heterogeneous distribution. This observation aligns with MgO's significantly smaller NPs dimensions, leading to a substantially higher surface-to-volume ratio. Despite this clustered distribution, the incorporated MgO nanoparticles may contribute to improved absorption and anti-inflammatory benefits, though these effects might be concentrated in regions with higher nanoparticle density. These distribution characteristics can significantly

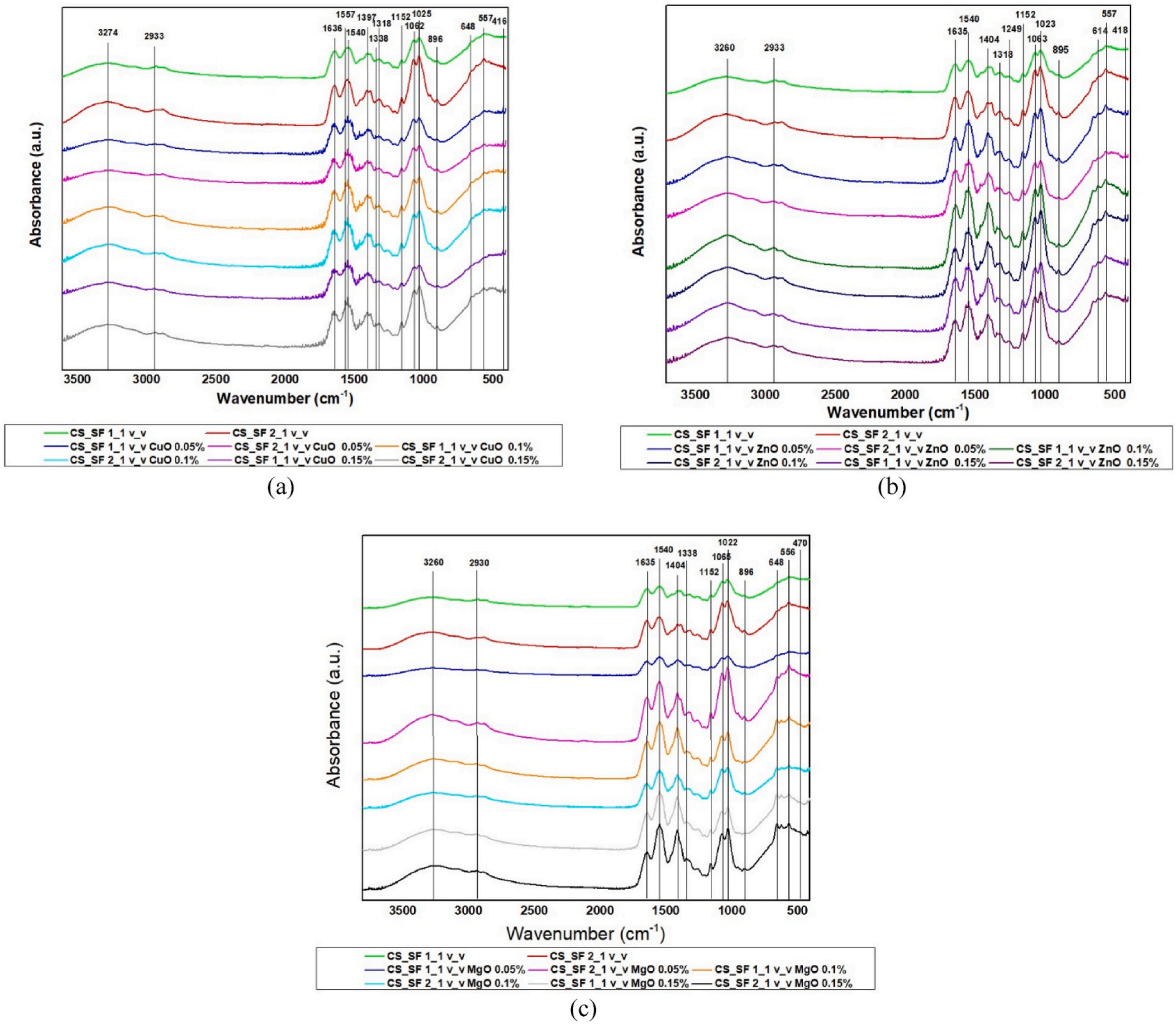

Fig. 7. FT-IR spectra of (a) CS/SF scaffolds containing green synthesized CuO NPs, (b) CS/SF scaffolds containing green synthesized ZnO NPs and (c) CS/SF scaffolds containing green synthesized MgO NPs. (For interpretation of the references to colour in this figure legend, the reader is referred to the Web version of this article.)

influence the mechanical, absorption, and antibacterial properties of the scaffolds, with potential consequences for their performance in wound healing applications. The increased oxygen content at the scaffold edges (Fig. 6b–e,h) is attributed to structural, physicochemical, and environmental factors that influence oxygen distribution. In this direction, it is well known that the margins are more exposed, which allows quicker oxygen diffusion from the surrounding environment. This oxygen storage is also enabled by the hydrophilic nature of the ZnO, CuO, and MgO NPs, which capture and retain oxygen molecules on their surfaces. Furthermore, the scaffold's porous structure, which includes larger, more open pores at the outer edges, encourages oxygen accumulation. Increased NP concentrations can also cause edge aggregation, which increases oxygen accumulation. Additionally, chemical interactions—such as oxygen atoms on NP surfaces and hydrogen bonding between biopolymers and oxygen—are stronger toward the margins, adding to the increased oxygen present.

3.3. Fourier-transform infrared (FTIR) spectroscopy analysis

Fig. 7 show the results of an FTIR analysis conducted to further investigate the scaffold's functional groups and their interactions with the included green metal oxide NPs. Thus, specific absorption peaks can provide information about their integration inside the scaffold matrix. SF has various distinctive peaks linked with its protein structure. The amide I band at 1652 cm^{-1} is associated with the C=O stretching of the peptide backbone, indicating the random coil structure of SF [43]. Further, the peak of the amide II band at 1530 cm^{-1} is attributed to N-H bending vibrations, which are fundamental to the β-sheet and random coil conformations of the SF. The amide III band at 1250 cm^{-1} highlights C-N stretching and N-H deformation, validating the secondary structure of SF [44]. These peaks confirm the structural integrity and protein-based origin of SF inside the scaffold [43,45]. Chitosan-specific functional groups were identified within the spectra as follows: the hydroxyl (OH) stretching band at 3270 cm^{-1} is a representative group of the extensive hydrogen bonding present in CS, as well as its polysaccharide structure. The absorption peak at 2917 cm^{-1} is attributed to the C-H stretching vibration, which corresponds to the aliphatic chains in CS [43,46]. Similar to SF, the amide II band around 1530 cm^{-1} may be attributed to N-H bending. In addition, the two absorption bands at 1085 cm^{-1} and 1415 cm^{-1} have been assigned to the C-O stretching vibrations [47]. This reflects the saccharide units in chitosan, indicating its polysaccharide backbone. These peaks demonstrate the chemical presence of CS within the scaffold and its impact on the matrix [48]. Moreover, the peaks observed in the range of 450–550 cm^{-1} have been correlated with the metal-oxide-related groups, associated with O-Zn-O groups, Cu-O stretching vibrations [49], and Mg-O vibrations [50], demonstrating interactions between the NPs and the matrix of biopolymers [51]. Furthermore, the presence of ZnO, CuO, and MgO NPs influenced the functional group vibrations of both CS and SF (slight shift, broadening), implying a possible link between the NPs and the

Table 2
Identified compounds in *Citrus sinensis* extract and their roles [52–55].

Compound Class	Specific Compounds	Role in NP Synthesis	Additional Notes
Terpenoids	Linalool	Reducing agent (via –OH groups)	Contributes to NP stabilization
	α-Terpineol	Chelate metal ions	Enhances NP morphology
	Carvone	Antioxidant properties	May influence NP size distribution
	Nootkatone	Stabilizes NP surface	Found in trace amounts
Methoxyflavones	Tangeretin	Strong reductant (polyphenolic structure)	Key for Zn^{2+}/ Cu^{2+} reduction
	Nobiletin	Metal ion chelation	Improves NP dispersity
	Heptamethoxyflavone	Crosslinking potential	Detected at high temps (>300 °C)
Fatty Acids	Palmitic acid	Capping agent (forms micelles)	Affects NP hydrophobicity
	Linoleic acid	Stabilizes colloidal NPs	May reduce aggregation
	Oleic acid	Surfactant-like behavior	Linked to a smaller NP size
	Stearic acid	Modifies surface energy	Impacts on scaffold integration
Amino Acids/ Sugars	(Derivatized with BSTFA)	Potential NP morphology modifiers	Requires further biocompatibility studies

hydroxyl (OH) or amide groups of CS and SF. This connection is critical for the scaffold's structural integrity and improved functionality.

Furthermore, the FTIR analysis presented valuable information about the molecular interactions between the metal oxide NPs and the biopolymer matrix. Several key spectral regions showed increased band intensities with higher NP concentrations. In addition, the hydroxyl stretching region (3200-3400 cm^{-1}, centered at 3270 cm^{-1}) showed a progressive intensity increase, indicating stronger hydrogen bonding networks formed between the NPs and the -OH groups of both CS and SF. In addition, enhanced intensities in the amide I (1630-1680 cm^{-1}) and amide II (1510-1550 cm^{-1}) band regions indicate the successful interactions between the metal ions and the functional groups of the SF, which might affect SF's secondary structure. Moreover, the C-O stretching vibrations between 1050 and 1100 cm^{-1} had been significantly enhanced, in particular the peak at 1085 cm^{-1}, demonstrating the interaction between metal ions and oxygen atoms in the chitosan saccharide units. Therefore, the FTIR spectra indicate that metal oxide NPs function as crosslinking agents within the matrix of the scaffold. In this regard, the metal ions (Zn^{2+}, Cu^{2+}, Mg^{2+}) form coordination bonds with electronegative groups (such as -OH, -NH_2, and C=O) in both CS and SF, resulting in a reinforced three-dimensional network. The progressive variations in spectrum intensities as the concentration of the NP increases suggest a concentration-dependent effect on scaffold structure.

3.4. Phytochemical profile and functional role in nanoparticle synthesis

The GC-MS analysis of the *Citrus sinensis* (orange peel) extract confirms the presence of bioactive compounds that are critical for the green synthesis of metal oxide NPs, as shown in Table 2. In this regard, the analysis revealed the presence of volatile organic compounds, including terpenoids (linalool, α-terpineol, carvone, nootkatone) and methoxyflavones (tangeretin, nobiletin), which are known to act as reducing and stabilizing agents in nanoparticle synthesis due to their hydroxyl (–OH) and carbonyl (C=O) functional groups. Furthermore, fatty acids such as palmitic, linoleic, oleic, and stearic acids have been found, which could

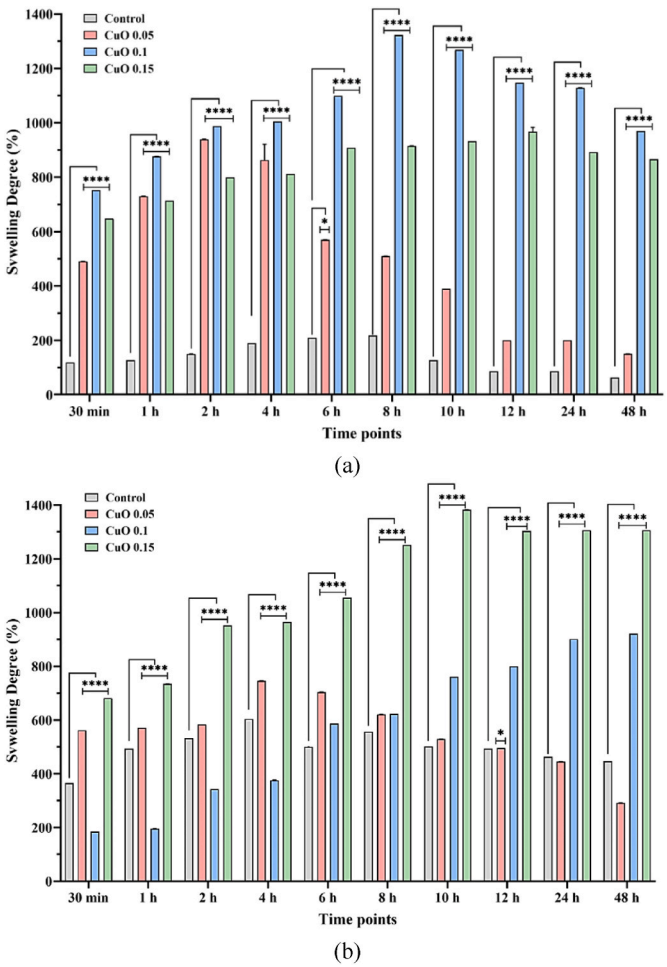

Fig. 8. Swelling degree of chitosan/silk fibroin scaffolds containing green-synthesized CuO nanoparticles at (a) 1:1 and (b) 2:1 CS/SF ratios. Statistical analysis was performed using two-way ANOVA followed by Tukey and Holm-Šidák's multiple comparisons tests. Results were considered statistically significant at $^{*}p < 0.0063$, $^{****}p < 0.0001$ for (a) and $^{*}p < 0.0016$, $^{**}p < 0.0001$ for (b) ($n = 3$). (For interpretation of the references to colour in this figure legend, the reader is referred to the Web version of this article.)

contribute to NP capping and colloidal stability. Further investigation of the derivatized aqueous phase revealed amino acids and sugars that could affect NP shape or scaffold biocompatibility. Terpenoids and methoxyflavones play a crucial role in reducing metal ions (Zn^{2+}, Cu^{2+}, Mg^{2+}) during green synthesis. Fatty acids may also act as surfactants to control nanoparticle size and dispersion. Even though GC-MS showed the presence of reducing agents (e.g., limonene, flavonoids) in the orange peel extract, our next research will involve a quantitative assessment (e.g., HPLC) to connect specific phytochemical quantities with NP characteristics and ensure batch-to-batch consistency.

3.5. Swelling degree assessment

The developed scaffolds' swelling degree (SD) evaluation was performed to assess their suitability for the targeted application. Hence, it was concluded that the SD characteristics could vary depending on both the type and concentration of the green-synthesized metal oxide NPs incorporated into the obtained scaffolds [56]. Additionally, swelling behavior reflects the scaffold's ability to absorb and retain water and suggests its degradation over time. The control group, which consisted of scaffolds lacking NPs (shown in Figs. 7–10), displayed a small SD throughout the research. In this manner, the early swelling is mild, beginning at 242 % and reaching a maximum SD of 397 % after 4 h.

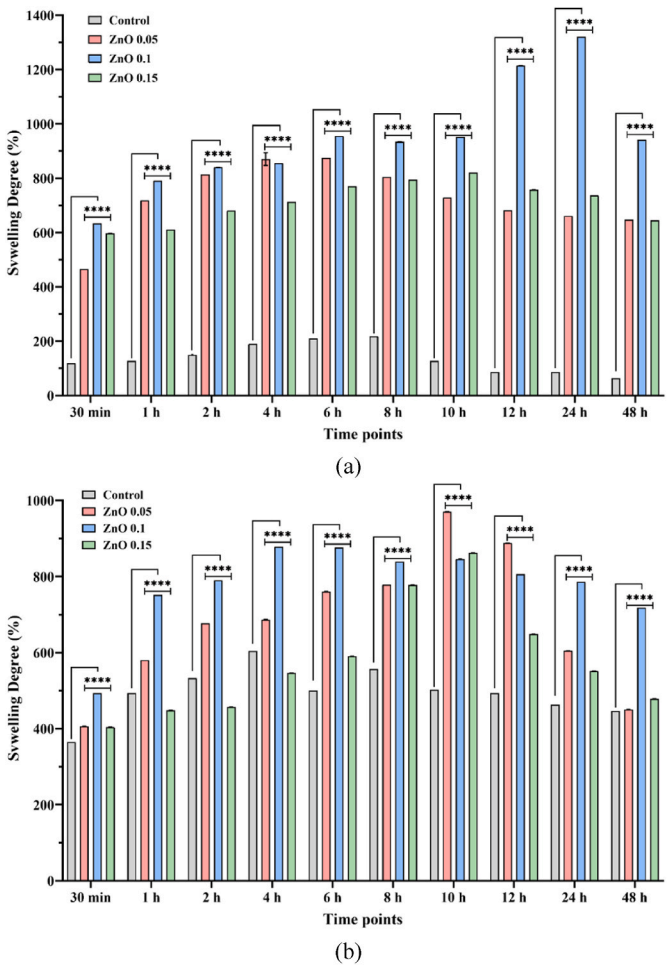

Fig. 9. Swelling degree of chitosan/silk fibroin scaffolds containing ZnO nanoparticles at (a) 1:1 and (b) 2:1 CS/SF ratios. Statistical analysis was performed using two-way ANOVA followed by Tukey and Holm-Šidák's multiple comparisons tests. Results were considered statistically significant at $^{**}p < 0.0001$ ($n = 3$).

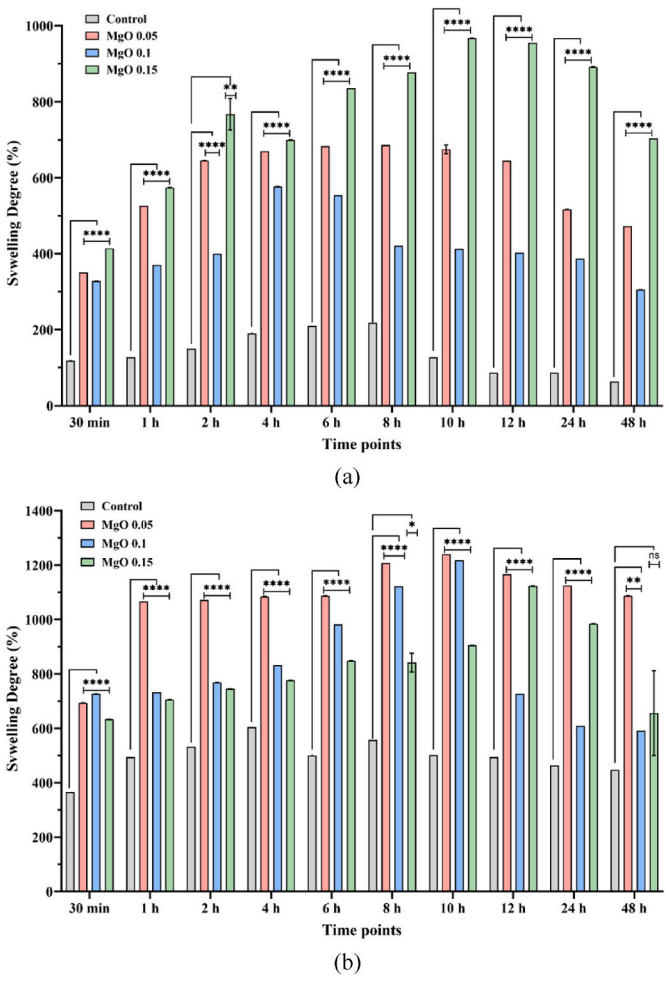

Fig. 10. Swelling degree of chitosan/silk fibroin scaffolds containing green-synthesized MgO nanoparticles at (a) 1:1 and (b) 2:1 CS/SF ratios. Statistical analysis was performed using two-way ANOVA followed by Tukey and Holm-Šidák's multiple comparisons tests. Results were considered statistically significant at $^{**}p < 0.0032$, $^{****}p < 0.0001$ for (a) and $^{*}p < 0.0122$, $^{**}p < 0.0032$, $^{**}p < 0.0001$ for (b) ($n = 3$). (For interpretation of the references to colour in this figure legend, the reader is referred to the Web version of this article.)

Further, swelling gradually reduces with time, demonstrating limited water absorption capacity and a lack of improved structural characteristics generally provided by NPs. Therefore, the control samples highlight the essential role of NPs in improving water uptake and retention. Without NPs, the scaffolds lack the porosity and crosslinking stability needed for effective biomedical applications, particularly in wound healing [32].

Moreover, as illustrated in Fig. 7, CS/SF CuO NPs scaffolds demonstrated balanced and unique swelling behavior. At first, the SD increases moderately, from 553 % to 637 % within the 1st h, reflecting a controlled interaction between CuO NPs and the scaffold matrix. This moderate water uptake continues, reaching a maximum SD at approximately 821 % after 6 h. Unlike CS/SF ZnO NPs and CS/SF MgO NPs scaffolds, CS/SF CuO NPs scaffolds have shown the most stable swelling behavior. By 12 h, the swelling degree remains steady at around 822 %, with minimal decrease even after 48 h. This stability suggests that CuO NPs reinforce crosslinking while maintaining sufficient porosity for water retention. The lack of significant reduction in swelling over time could imply a slower degradation compared to CS/SF ZnO NPs and CS/SF MgO NPs scaffolds. This constant and moderate swelling makes CS/SF CuO NPs scaffolds is suitable for applications that require balanced hydration without rapid breakdown, such as wound management over medium to long periods.

As shown in Fig. 9, CS/SF ZnO NPs scaffolds demonstrated distinct

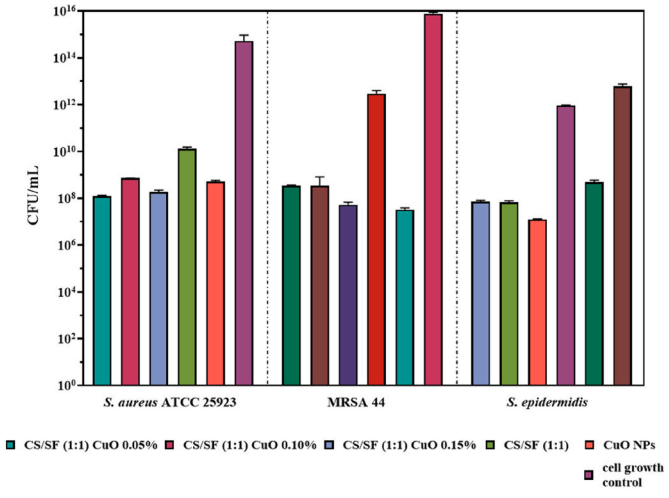

Fig. 11. The influence of the CS/SF 1:1-CuO NPs scaffolds. Statistical analysis was performed using ANOVA with Tukey's/Holm-Šídák's multiple comparisons test. Differences were considered statistically significant at $p < 0.05$ ($n = 3$).

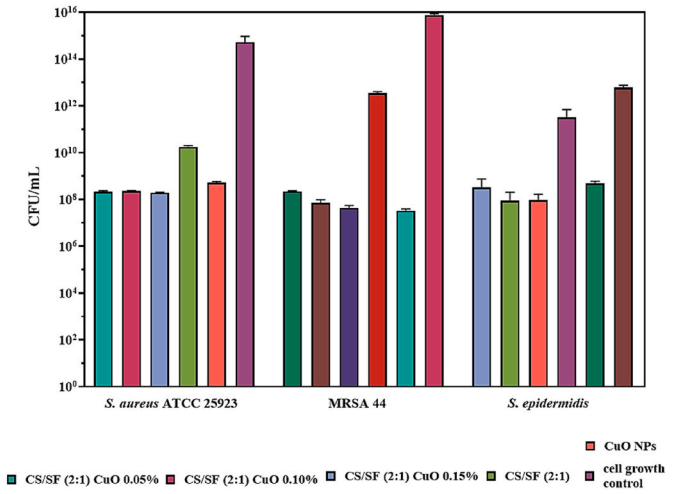

Fig. 12. The influence of the CS/SF 2:1-CuO NPs scaffolds. Statistical analysis was performed using ANOVA with Tukey's/Holm-Šídák's multiple comparisons test. Differences were considered statistically significant at $p < 0.05$ ($n = 3$).

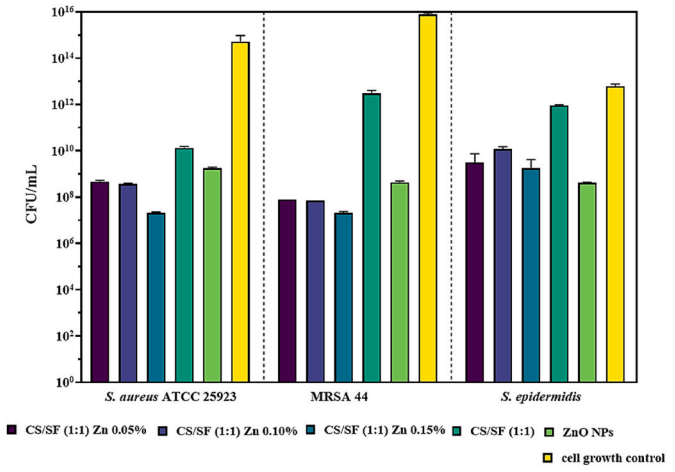

Fig. 13. The influence of the CS/SF 1:1-ZnO NPs scaffolds. Statistical analysis was performed using ANOVA with Tukey's/Holm-Šídák's multiple comparisons test. Differences were considered statistically significant at $p < 0.05$ ($n = 3$).

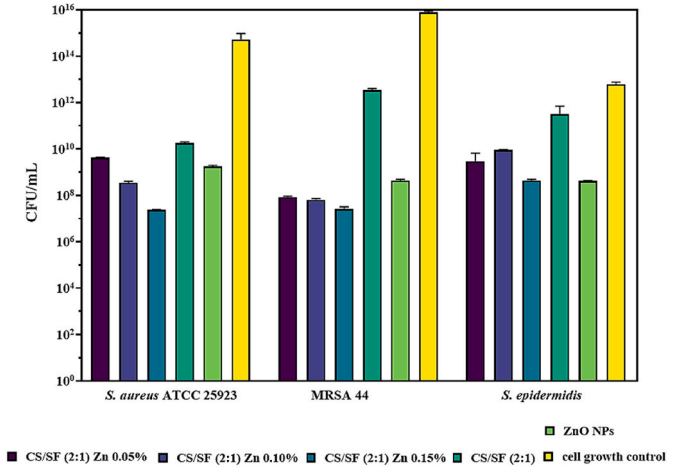

Fig. 14. The influence of the CS/SF 2:1-ZnO NPs scaffolds. Statistical analysis was performed using ANOVA with Tukey's/Holm-Šídák's multiple comparisons test. Differences were considered statistically significant at $p < 0.05$ ($n = 3$).

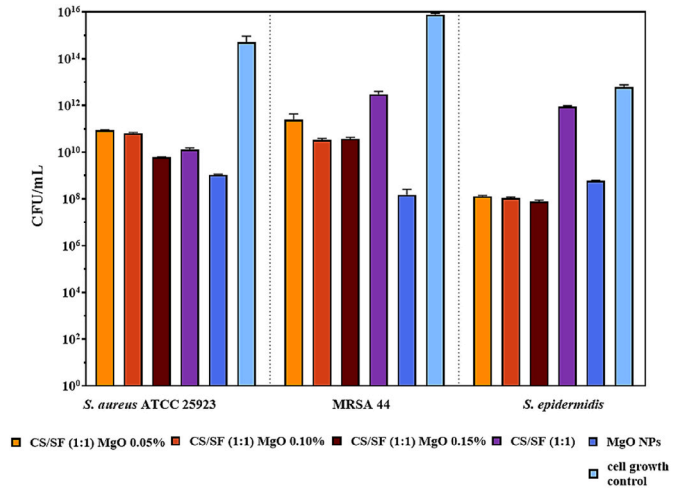

Fig. 15. The influence of the CS/SF 1:1 -MgO NPs scaffolds. Statistical analysis was performed using ANOVA with Tukey's/Holm-Šídák's multiple comparisons test. Differences were considered statistically significant at $p < 0.05$ ($n = 3$).

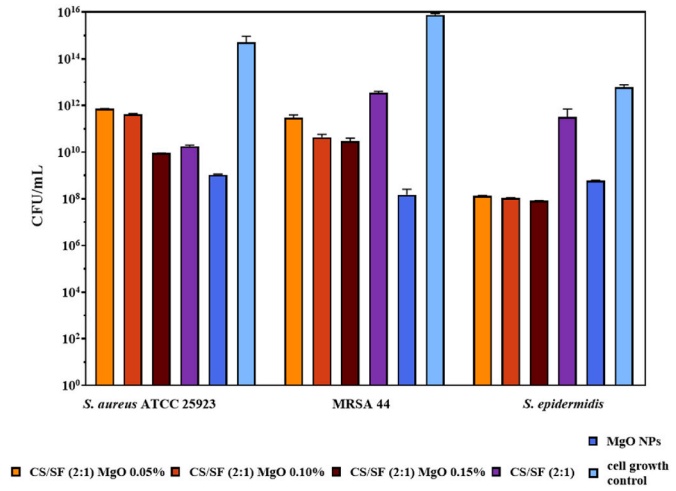

Fig. 16. The influence of the CS/SF 2:1 -MgO NPs scaffolds. Statistical analysis was performed using ANOVA with Tukey's/Holm-Šídák's multiple comparisons test. Differences were considered statistically significant at $p < 0.05$ ($n = 3$).

swelling behavior across multiple phases. In the beginning, they demonstrated significant water uptake, with SDs increasing from 500 % to 650 % within the 1st h, which was attributed to ZnO's hydrophilic nature. After 4 h, the SD reached ~2094 %, which was significantly higher than for all other samples examined. This exceptional increase could therefore be attributed to the ZnO NPs interaction with the scaffold matrix, which may disrupt crosslinking and temporarily enhance porosity [57]. However, the composite scaffolds showed poor long-term stability, with a continuous SD decrease to 833 % at 12 h and finally to 647 % by 48 h. This reduction can therefore be associated with both saturation of water absorption sites and progressive scaffold degradation, compromising the structure's water retention capacity [58]. Therefore, the ZnO NPs-incorporated composite scaffolds could be selected only for applications requiring rapid initial hydration, such as acute wound care, their accelerated degradation profile making them less suitable for extended therapeutic applications.

In contrast to ZnO NPs, MgO NPs have exhibited more controlled and sustained swelling behavior (Fig. 10). The initially observed behavior shows a moderate increase in swelling from 524 % to 663 % within the 1st h. Furthermore, the swelling profile reaches a maximum of 837 % at 12 h, much later than CS/SF ZnO NPs, indicating progressive and

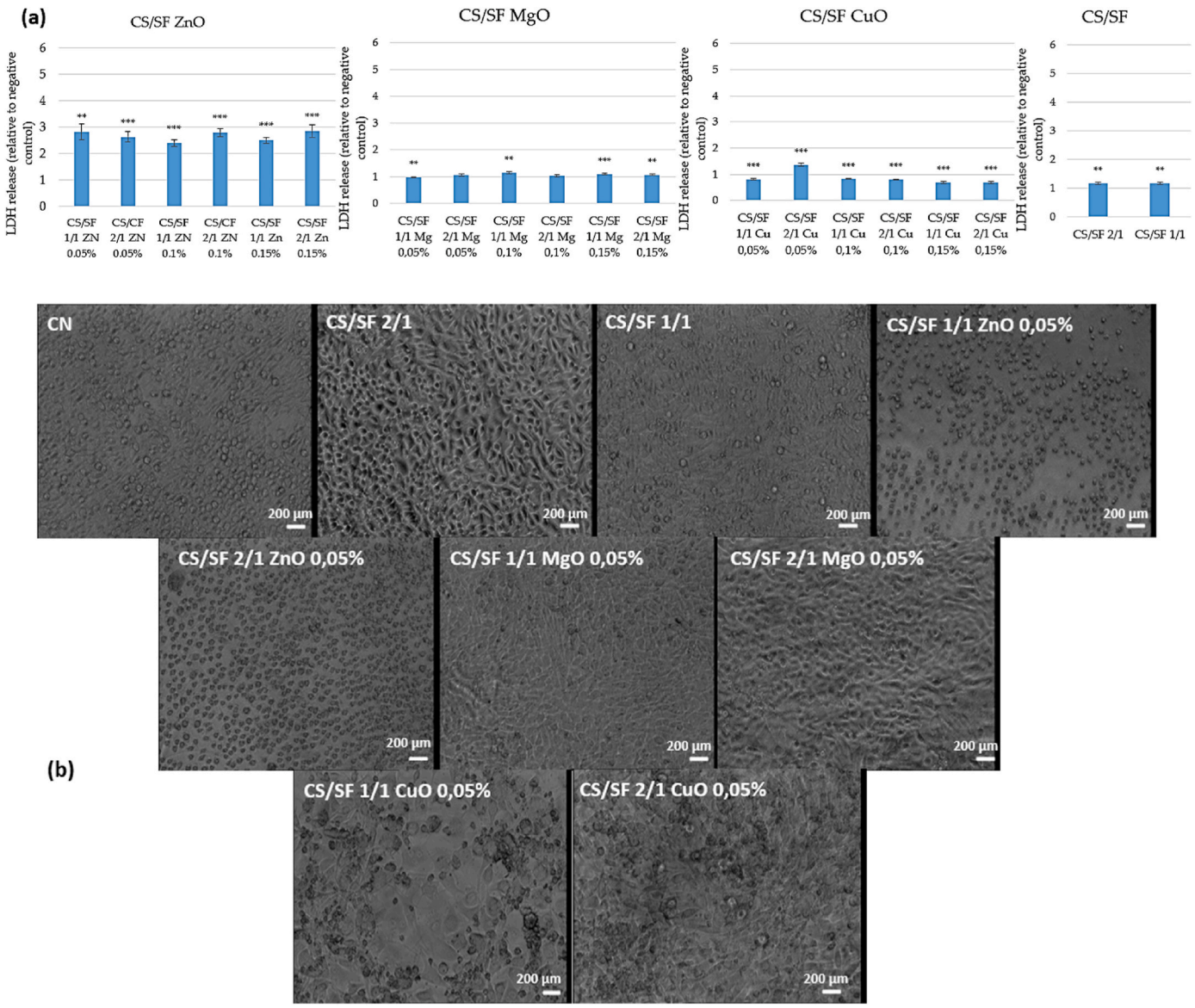

Fig. 17. (a) LDH release from fibroblast cells incubated with CS/SF scaffolds loaded with ZnO, CuO, and MgO NPs. Error bars represent standard deviation ($n = 3$). Asterisks denote significant differences compared to the control (*p < 0.05, **p < 0.01, ***p < 0.001) and (b) Optical microscopy images of fibroblast cell morphology following exposure to the scaffold samples, showing cell density, shape, and attachment behavior.

Table 3
Morphological impact of NPs on CS/SF scaffolds.

NP Type	0.05 % Dispersion	0.15 % Dispersion	Optimal CS/SF Ratio
ZnO	Homogeneous, minimal aggregation	Increased aggregation, denser zones	1:1 (enhanced porosity)
MgO	Moderate dispersion, some clustering	Severe aggregation, irregular pores	1:1 (better uniformity)
CuO	Well-dispersed, uniform pores	Minimal aggregation, stable structure	1:1 ≈ 2:1 (balanced)

prolonged water absorption. The subsequent swelling decreased to 651 % within 48 h, demonstrating minimal degradation and improved structural integrity over time.

The CS/SF MgO NPs scaffolds demonstrated a gradual and sustained swelling profile, reaching maximum values at later time points compared to other formulations. This behavior reflects a slower fluid uptake rate and improved structural stability over time. Although this does not equate to direct hydration of the wound, such absorption characteristics can be beneficial in managing wound exudate and maintaining a moist environment in the early stages of healing. Chronic wounds are considered a significant public health problem due to their association with infections and the ability of pathogenic microorganisms to generate biofilms, which, due to their complex architecture, are very resistant to antibiotics [59]. Therefore, this study presents alternative wound healing treatments using CS/SF scaffolds and ZnO, CuO, and MgO NPs as bioactive agents. A significant inhibitory effect on the tested strains was observed for the scaffolds loaded with CuO NPs, as shown in Figs. 11 and 12. Generally, the CS/SF (1:1) scaffolds determined the highest sensitivity of the strains than CS/SF (2:1), and their ability to inhibit the adhesion of bacterial cultures increases with the concentration of CuO NPs. Furthermore, CS/SF-ZnO NPs scaffolds determined a significant sensitivity of all strains tested in this study. The inhibitory effect can be observed in Figs. 13 and 14, with a significant decrease (more than 4 log CFU/mL) for all samples compared to cell growth controls. The clinically isolated MRSA 44 presented the highest sensitivity, followed by *S. aureus* ATCC 25923 and *S. epidermidis*. Moreover,

Table 4
Water uptake behavior of CS/SF scaffolds containing different types of metal oxide NPs.

NP Type	Initial Swelling	Maximum Swelling	Stabilization	Degradation Indication	Mechanism	Application
ZnO	quick (~650 %)	very quick (~2094 %)	decreased (~647 %)	faster degradation	hydrophilicity and pore disruption for rapid uptake.	acute wound care, which requires rapid hydration
MgO	moderate (~663 %)	high (~837 %)	stable (~651 %)	moderate degradation	controlled porosity and stable interactions.	chronic wounds with sustained hydration need
CuO	moderate (~637 %)	moderate (~821 %)	stable (~822 %)	slower degradation	balanced crosslinking and moderate porosity.	balanced hydration for longer wound management
Control	slow (~242 %)	slow (~397 %)	limited (~300 %)	significant structural limitations	minimal porosity and water interaction.	baseline comparison; is not ideal for clinical use

Table 5
Comprehensive antibacterial performance and clinical guidance of CS/SF scaffolds.

NP	Concentration	MRSA 44 Reduction (log CFU/mL)	*S. aureus* ATCC 25923 Reduction (log CFU/mL)	*S. epidermidis* Reduction (log CFU/mL)	Activity Mechanism	Recommended Clinical Application
ZnO	0.05 %	2.1 ± 0.2	1.8 ± 0.3	1.5 ± 0.2	ROS generation, membrane damage, and zinc ion release	Mild infections requiring rapid action
	0.1 %	3.4 ± 0.3	3.0 ± 0.2	2.6 ± 0.3		Moderate MRSA/ *S. aureus* infections
	0.15 %	4.3 ± 0.2	3.8 ± 0.3	3.2 ± 0.4		Severe/resistant infections
CuO	0.05 %	1.5 ± 0.2	1.3 ± 0.1	1.6 ± 0.2	Copper ion release, sustained ROS production	Prophylactic coverage
	0.1 %	2.3 ± 0.3	2.0 ± 0.2	2.2 ± 0.3		Chronic wound maintenance
	0.15 %	3.0 ± 0.3	2.7 ± 0.2	2.9 ± 0.3		Infected chronic wounds
MgO	0.05 %	0.8 ± 0.1	0.6 ± 0.1	1.2 ± 0.2	Alkalinization, physical membrane disruption	*S. epidermidis* colonization
	0.1 %	1.4 ± 0.2	1.1 ± 0.1	2.0 ± 0.2		Biofilm-prone wounds
	0.15 %	1.5 ± 0.2	1.2 ± 0.1	2.1 ± 0.2		Refractory biofilm cases
Control	0 %	0.4 ± 0.1	0.6 ± 0.1	0.5 ± 0.1	Chitosan's weak cationic effect	Non-infected wound coverage

the scaffolds loaded with the highest concentration of ZnO NPs (0.15 %) presented the highest antibacterial effect/ability to inhibit the adhesion of bacterial cultures on their surfaces. In addition, the CS/SF (1:1) determined a more pronounced inhibitory effect than CS/SF (2:1).

Figs. 15 and 16 illustrate the effect of CS/SF scaffolds loaded with MgO on the tested Gram-positive bacteria. MgO NPs significantly decreased the adherence of *S. epidermidis*. Furthermore, all samples demonstrated a synergistic effect of CS, SF, and MgO NPs. Similarly, adding MgO NPs increases the antibacterial activity of the scaffolds, except in the case of *S. aureus* ATCC 25923. The high degree of inhibition for the studied bacterial strains and their low capacity to adhere to the surface of the CS/SF membranes make the samples studied to be used as an alternative in wound dressing treatment.

3.6. Cytotoxicity evaluation

As shown in Fig. 17, the LDH assay evaluates the cytotoxicity of the scaffold samples following the release of Lactate Dehydrogenase, a cytosol-specific enzyme, in the extracellular medium. This is a measure of cell membrane lysis. LDH release following fibroblast cells incubation in the presence of the scaffold samples was calculated relative to the negative control, and determinations confirmed the biocompatibility of the CS/SF control samples, but also of the scaffolds loaded with MgO and CuO nanoparticles. In case of CS/SF scaffolds loaded with ZnO nanoparticles, the released LDH quantity increased up to 3 times compared to the negative control at 7 days of incubation, an effect determined by a mechanism dependent on the lesions of the cell membrane.

4. Discussion

This study effectively created chitosan/silk fibroin (CS/SF) scaffolds that contained green-synthesized ZnO, CuO, and MgO NPs, displaying customized properties for wound healing applications. SEM analysis revealed that NP type and concentration critically influence scaffold porosity (Table 3). At 0.05 % w/w, all NPs (ZnO, CuO, MgO) were dispersed uniformly, preserving structural integrity. Higher concentrations (0.15 %) induced aggregation, particularly for MgO, reducing pore homogeneity. The 1:1 CS/SF ratio outperformed 2:1 in porosity and NP distribution, aligning with prior studies [60,61].

Related to the swelling and degradation dynamics, the scaffolds containing ZnO NPs achieved rapid hydration (2094 % swelling at 4 h) but poor long-term stability due to matrix disruption, while CuO/MgO scaffolds sustained swelling (>800 % at 48 h) via reinforced crosslinking (Table 4). The 1:1 ratio enhanced water absorption, ideal for chronic wounds [62,63].

Furthermore, ZnO NPs showed the highest efficacy against MRSA (4.3 log CFU/mL reduction at 0.15 %) via ROS generation, whereas CuO NPs provided sustained activity through gradual ion release (Table 5). MgO NPs were less effective but synergized with CS/SF against *S. epidermidis* biofilms [64].

While this study demonstrated the scaffolds' excellent antibacterial activity and swelling behavior, mechanical properties such as tensile strength and elasticity were not evaluated, as the scaffolds were designed for short-term wound healing applications where these parameters are less critical. Future studies could explore mechanical characterization for scaffolds intended for long-term or load-bearing applications. These findings show that CS/SF scaffolds containing green-synthesized ZnO, CuO, and MgO NPs are attractive candidates for advanced wound dressings, since they combine good swelling behavior with strong antibacterial activity. The most balanced formulation, with a 1:1 CS/SF ratio and 0.1 % NPs, provided structural integrity as well as biological functionality. The next phase of research should concentrate on in vivo examination of wound healing efficacy in preclinical models, the development of hybrid NP systems combining multiple metal oxides for synergistic effects, the integration of 3D bioprinting techniques for customized scaffold architectures, and the clinical application of these

eco-friendly nanocomposites. Such advances have the potential to narrow the gap between laboratory innovation and clinical application, whereas the green synthesis approach provides a long-term foundation for producing medical-grade biomaterials on a large scale.

5. Conclusions

This study successfully synthesized multifunctional CS/SF scaffolds containing green-synthesized ZnO, CuO, and MgO NPs for wound healing applications. The scaffolds displayed increased swelling capacity and antibacterial activity, particularly ZnO NPs, exhibiting higher hydrophilicity and fast hydration. On the other hand, the scaffolds containing CuO and MgO NPs offered sustained swelling and stability. The 1:1 CS/SF ratio surpassed the 2:1 ratio in terms of porosity, water absorption, and antibacterial activity, especially against *Staphylococcus aureus* and MRSA. Optimal NP concentrations (0.1 % w/w) achieved a balance between structural integrity and biological functioning. Future studies should concentrate on in vivo testing to confirm biocompatibility and wound healing performance, as well as hybrid NP systems and 3D bioprinting for customized scaffold structures. These eco-friendly nanocomposites show great promise for clinical translation, addressing the limitations of traditional wound dressings.

CRediT authorship contribution statement

Denisa-Maria Radulescu: Writing – original draft, Investigation, Formal analysis. **Bodgan Stefan Vasile:** Writing – review & editing, Validation, Supervision, Project administration. **Vasile-Adrian Surdu:** Formal analysis, Data curation. **Roxana-Doina Trusca:** Data curation. **Cornelia-Ioana Ilie:** Formal analysis. **Roxana Cristina Popescu:** Writing – original draft, Investigation, Formal analysis, Data curation. **Ecaterina Andronescu:** Supervision, Project administration. **Veronica Drumea:** Investigation, Formal analysis, Data curation. **Lia-Mara Ditu:** Data curation.

Data availability

The original contributions presented in this study are included in the article/supplementary material. Further inquiries can be directed to the corresponding author(s).

Declaration of competing interest

The authors declare that they have no known competing financial interests or personal relationships that could have appeared to influence the work reported in this paper.

Acknowledgment

The authors are grateful to the Romanian Government for providing access to the research infrastructure of the National Center for Micro and Nanomaterials through the National Program titled “Installations and Strategic Objectives of National Interest”.

Appendix A. Supplementary data

Supplementary data to this article can be found online at https://doi.org/10.1016/j.jddst.2025.107463.

References

[1] J. Tian, C. Fu, W. Li, N. Li, L. Yao, J. Xiao, Biomimetic tri-layered artificial skin comprising silica gel-collagen membrane-collagen porous scaffold for enhanced full-thickness wound healing, Int. J. Biol. Macromol. 266 (2024) 131233.
[2] C. Zhao, L. Huang, J. Tang, L. Lv, X. Wang, X. Dong, F. Yang, Q. Guan, Multifunctional nanofibrous scaffolds for enhancing full-thickness wound healing loaded with Bletilla striata polysaccharides, Int. J. Biol. Macromol. 278 (2024) 134597.
[3] S. Muneeb Haider Gillani, A. Mughal, R. Ahmed Malik, H. Alrobei, I. AlBaijan, M. Atiq Ur Rehman, Development of 3D printed sodium alginate/agar-agar/cloves scaffolds for potential wound healing applications, Mater. Lett. 377 (2024) 137357.
[4] N. Poddar, D. Chonzom, S. Sen, Malsawmtluangi, N. Parihar, P.M. Patil, J. Balani, S.M. Upadhyayula, D.B. Pemmaraju, Biocompatible arabinogalactan-chitosan scaffolds for photothermal pharmacology in wound healing and tissue regeneration, Int. J. Biol. Macromol. 268 (2024) 131837.
[5] K. Mukai, T. Nakatani, Comparison of different modern wound dressings on full-thickness murine cutaneous wound healing with wild-type and type-2 diabetes Db/Db mice, J. Tissue Viability (2024).
[6] M. Teng, X. Luo, F. Ao, L. Li, J. Feng, P. Zhang, X. Zhang, X. Liu, C. Yang, L. Ji, X. Wang, H. Ju, X. Liu, Silk-fibroin-based nanofibrous scaffolds integrated with nano-engineered living bacteria enabling antibiotic-free accelerated infected wound healing, Chem. Eng. J. 496 (2024) 154233.
[7] K. Cheng, Y. Deng, L. Qiu, S. Song, L. Chen, L. Wang, Q. Yu, Heparin-loaded hierarchical fiber/microsphere scaffolds for anti-inflammatory and promoting wound healing, Smart Mater. Med. 5 (2) (2024) 240–250.
[8] B. Wang, Y. Lang, C. Li, S. Liu, M.-W. Chang, Biomimetic 3D composite scaffold with pH-Responsive micropatterns for wound healing, Chem. Eng. J. 485 (2024) 149646.
[9] M.A.F. Maghsoudi, R.M. Aghdam, R.A. Asbagh, A. Moghaddaszadeh, A. Ghaee, S. M.A. Tafti, L. Foroutani, S.H.A. Tafti, 3D-printing of alginate/gelatin scaffold loading tannic acid@ZIF-8 for wound healing: in vitro and in vivo studies, Int. J. Biol. Macromol. 265 (2024) 130744.
[10] R. Narayanam, L.M. Cardoso, A.H. dos Reis-Prado, A.B.G. de Carvalho, C. Anselmi, A.H. Mahmoud, J.C. Fenno, R. Dal-Fabbro, M.C. Bottino, Antimicrobial silk fibroin methacrylated scaffolds for regenerative endodontics, J. Endod. (2024).
[11] M. Li, X. Cao, H. Zhang, A. Li, W. Zhou, Y. Wu, Y. Zheng, Improved biocompatibility and osteogenesis of porous graphene oxide/silk fibroin scaffold for potential applications in bone tissue engineering, Mater. Today Commun. 40 (2024) 109480.
[12] Z. Bashiri, A.M. Sharifi, M. Ghafari, S.J. Hosseini, Z. Shahmahmoodi, A. Moeinzadeh, H. Parsaei, F. Khadivi, A. Afzali, M. Koruji, In-vitro and in-vivo evaluation of angiogenic potential of a novel lithium chloride loaded silk fibroin/alginate 3D porous scaffold with antibacterial activity, for promoting diabetic wound healing, Int. J. Biol. Macromol. 277 (2024) 134362.
[13] R.S. Khan, A.H. Rather, T.U. Wani, S.u. Rather, A. Abdal-hay, F.A. Sheikh, A comparative review on silk fibroin nanofibers encasing the silver nanoparticles as antimicrobial agents for wound healing applications, Mater. Today Commun. 32 (2022) 103914.
[14] H. Motasadizadeh, M. Tavakoli, S. Damoogh, F. Mottaghitalab, M. Gholami, F. Atyabi, M. Farokhi, R. Dinarvand, Dual drug delivery system of teicoplanin and phenamil based on pH-sensitive silk fibroin/sodium alginate hydrogel scaffold for treating chronic bone infection, Biomater. Adv. 139 (2022) 213032.
[15] S. Niveditha, V.T. Veetil, A.D. Rajeeve, S. Cheriyan, R. Yamuna, M. Karthega, Wound healing applications of β-cyclodextrin capped zinc sulphide nanoparticles impregnated electrospun polymeric nanofibrous scaffold, J. Drug Deliv. Sci. Technol. 95 (2024) 105597.
[16] P.-K.T. Ngo, D.N. Nguyen, H.-P. Nguyen, T.-H.H. Tran, Q.-N.D. Nguyen, C.H. Luu, T.-H. Phan, P.K. Le, V.H.G. Phan, H.T. Ta, T. Thambi, Silk fibroin/chitosan/montmorillonite sponge dressing: enhancing hemostasis, antimicrobial activity, and angiogenesis for advanced wound healing applications, Int. J. Biol. Macromol. 279 (2024) 135329.
[17] S. Narayana, A. Nasrine, M. Gulzar Ahmed, R. Sultana, B.H. Jaswanth Gowda, S. Surya, M. Almuqbil, S.M.B. Asdaq, S. Alshehri, S. Arif Hussain, Potential benefits of using chitosan and silk fibroin topical hydrogel for managing wound healing and coagulation, Saudi Pharm. J. 31 (3) (2023) 462–471.
[18] M.H. Kazemi, S. Sajadimajd, Z. Gorgin Karaji, In vitro investigation of wound healing performance of PVA/chitosan/silk electrospun mat loaded with deferoxamine and ciprofloxacin, Int. J. Biol. Macromol. 253 (2023) 126602.
[19] Z. Jiang, B. Liu, L. Yu, Y. Tong, M. Yan, R. Zhang, W. Han, Y. Hao, L. Shangguan, S. Zhang, W. Li, Research progresses in preparation methods and applications of zinc oxide nanoparticles, J. Alloys Compd. 956 (2023) 170316.
[20] L. Motelica, O.-C. Oprea, B.-S. Vasile, A. Ficai, D. Ficai, E. Andronescu, A. M. Holban, Antibacterial activity of solvothermal obtained ZnO nanoparticles with different morphology and photocatalytic activity against a dye mixture: methylene blue, rhodamine B and methyl Orange, Int. J. Mol. Sci. 24 (6) (2023) 5677.
[21] S.A. Akintelu, A.S. Folorunso, A review on green synthesis of zinc oxide nanoparticles using plant extracts and its biomedical applications, BioNanoScience 10 (4) (2020) 848–863.
[22] B.A. Khairnar, H.A. Dabhane, R.S. Dashpute, M.S. Girase, P.M. Nalawade, V. B. Gaikwad, Study of biogenic fabrication of zinc oxide nanoparticles and their applications: a review, Inorg. Chem. Commun. 146 (2022) 110155.
[23] J. Sackey, L.C. Razanamahandry, S.K.O. Ntwampe, N. Mlungisi, A. Fall, C. Kaonga, Z.Y. Nuru, Biosynthesis of CuO nanoparticles using Mimosa hamata extracts, Mater. Today Proc. 36 (2021) 540–548.
[24] C. Mendes, A. Thirupathi, M.E.A.B. Corrêa, Y. Gu, P.C.L. Silveira, The use of metallic nanoparticles in wound healing: new perspectives, Int. J. Mol. Sci. 23 (23) (2022) 15376.
[25] N. Thakur, J. Ghosh, S.K. Pandey, A. Pabbathi, J. Das, A comprehensive review on biosynthesis of magnesium oxide nanoparticles, and their antimicrobial, anticancer, antioxidant activities as well as toxicity study, Inorg. Chem. Commun. 146 (2022) 110156.

[26] G.M. Nair, T. Sajini, B. Mathew, Advanced green approaches for metal and metal oxide nanoparticles synthesis and their environmental applications, Talanta Open 5 (2022) 100080.
[27] J. Singh, T. Dutta, K.-H. Kim, M. Rawat, P. Samddar, P. Kumar, 'green' synthesis of metals and their oxide nanoparticles: applications for environmental remediation, J. Nanobiotechnol. 16 (1) (2018) 84.
[28] Naveen Priya, K. Kaur, A.K. Sidhu, Green synthesis: an eco-friendly route for the synthesis of iron oxide nanoparticles, Frontiers in Nanotechnology 3 (2021).
[29] A.u.R. Khan, K. Huang, Z. Jinzhong, T. Zhu, Y. Morsi, A. Aldalbahi, M. El-Newehy, X. Yan, X. Mo, Exploration of the antibacterial and wound healing potential of a PLGA/Silk fibroin based electrospun membrane loaded with zinc oxide nanoparticles, J. Mater. Chem. B 9 (5) (2021) 1452–1465.
[30] M. Kavousi Heidari, M. Pourmadadi, F. Yazdian, H. Rashedi, S.A.S. Ebrahimi, Z. Bagher, M. Navaei-Nigjeh, B.F. Haghirosadat, Wound dressing based on PVA nanofiber containing silk fibroin modified with GO/ZnO nanoparticles for superficial wound healing: in vitro and in vivo evaluations, Biotechnol. Prog. 39 (3) (2023) e3331.
[31] F. Paladini, F. Russo, A. Masi, C. Lanzillotti, A. Sannino, M. Pollini, Silver-treated silk fibroin scaffolds for prevention of critical wound infections, Biomimetics 9 (11) (2024) 659.
[32] D.-M. Radulescu, E. Andronescu, O.R. Vasile, A. Ficai, B.S. Vasile, Silk fibroin-based scaffolds for wound healing applications with metal oxide nanoparticles, J. Drug Deliv. Sci. Technol. 96 (2024) 105689.
[33] R. Eivazzadeh-Keihan, F. Khalili, H.A.M. Aliabadi, A. Maleki, H. Madanchi, E. Z. Ziabari, M.S. Bani, Alginate hydrogel-polyvinyl alcohol/silk fibroin/magnesium hydroxide nanorods: a novel scaffold with biological and antibacterial activity and improved mechanical properties, Int. J. Biol. Macromol. 162 (2020) 1959–1971.
[34] T.N.I.o.S.a. Technology, NIST chemistry WebBook. https://webbook.nist.gov. (Accessed 25 June 2025), 2025.
[35] G.M. Lemnaru Popa, L. Motelica, R.D. Trusca, C.I. Ilie, A.M. Croitoru, D. Ficai, O. Oprea, A. Stoica-Guzun, A. Ficai, L.M. Ditu, B.M. Tihăuan, Antimicrobial wound dressings based on bacterial cellulose and independently loaded with nutmeg and fir needle essential oils, Polymers 15 (17) (2023).
[36] A. Spoială, C.-I. Ilie, G. Dolete, A.-M. Croitoru, V.-A. Surdu, R.-D. Truşcă, L. Motelica, O.-C. Oprea, D. Ficai, A. Ficai, E. Andronescu, L.-M. Diţu, Preparation and characterization of Chitosan/TiO2 composite membranes as adsorbent materials for water purification, Membranes 12 (8) (2022) 804.
[37] G.M. Lemnaru Popa, R.D. Truşcă, C.I. Ilie, R.E. Ţiplea, D. Ficai, O. Oprea, A. Stoica-Guzun, A. Ficai, L.M. Diţu, Antibacterial activity of bacterial cellulose loaded with bacitracin and amoxicillin: in vitro studies, Molecules 25 (18) (2020).
[38] CLSI, Performance Standards for Antimicrobial Susceptibility TestingCLSI Supplement M100, Clinical and Laboratory Standards Institute, Berwyn, PA, USA, 2021.
[39] H. Veisi, B. Karmakar, T. Tamoradi, S. Hemmati, M. Hekmati, M. Hamelian, Biosynthesis of CuO nanoparticles using aqueous extract of herbal tea (Stachys lavandulifolia) flowers and evaluation of its catalytic activity, Sci. Rep. 11 (1) (2021) 1983.
[40] B.K. Sharma, D.V. Shah, D.R. Roy, Green synthesis of CuO nanoparticles using Azadirachta indica and its antibacterial activity for medicinal applications, Mater. Res. Express 5 (9) (2018) 095033.
[41] V. Harish, M.M. Ansari, D. Tewari, M. Gaur, A.B. Yadav, M.L. García-Betancourt, F. M. Abdel-Haleem, M. Bechelany, A. Barhoum, Nanoparticle and nanostructure synthesis and controlled growth methods, Nanomaterials 12 (18) (2022).
[42] K.A. Altammar, A review on nanoparticles: characteristics, synthesis, applications, and challenges, Front. Microbiol. 14 (2023).
[43] Q. Luo, Z. Chen, X. Hao, Q. Zhu, Y. Zhou, Preparation and properties of nanometer silk fibroin peptide/polyvinyl alcohol blend films for cell growth, Int. J. Biol. Macromol. 61 (2013) 135–141.
[44] S. Khosravimelal, M. Chizari, B. Farhadihosseinabadi, M. Moosazadeh Moghaddam, M. Gholipourmalekabadi, Fabrication and characterization of an antibacterial chitosan/silk fibroin electrospun nanofiber loaded with a cationic peptide for wound-dressing application, J. Mater. Sci. Mater. Med. 32 (9) (2021) 114.
[45] Y.R. Park, H.W. Ju, J.M. Lee, D.-K. Kim, O.J. Lee, B.M. Moon, H.J. Park, J.Y. Jeong, Y.K. Yeon, C.H. Park, Three-dimensional electrospun silk-fibroin nanofiber for skin tissue engineering, Int. J. Biol. Macromol. 93 (2016) 1567–1574.
[46] L. Dornjak, M. Kovačić, K. Ostojić, A. Angaits, J. Szpunar, I. Urlić, A. Rogina, Chitosan-boric acid scaffolds for doxorubicin delivery in the osteosarcoma treatment, Polymers 14 (21) (2022) 4753.
[47] D. Mukherjee, M. Azamthulla, S. Santhosh, G. Dath, A. Ghosh, R. Natholia, J. Anbu, B.V. Teja, K.M. Muzammil, Development and characterization of chitosan-based hydrogels as wound dressing materials, J. Drug Deliv. Sci. Technol. 46 (2018) 498–510.
[48] P.P. Patil, R.A. Bohara, J.V. Meshram, S.G. Nanaware, S.H. Pawar, Hybrid chitosan-ZnO nanoparticles coated with a sonochemical technique on silk fibroin-PVA composite film: a synergistic antibacterial activity, Int. J. Biol. Macromol. 122 (2019) 1305–1312.
[49] A. Chauhan, R. Verma, K. Batoo, Swati, R. Kalia, R. Kumar, M. Hadi, E. Raslan, A. Imran, Structural and optical properties of copper oxide nanoparticles: a study of variation in structure and antibiotic activity, J. Mater. Res. 36 (2021).
[50] N.K. Nga, N.T. Thuy Chau, P.H. Viet, Preparation and characterization of a chitosan/MgO composite for the effective removal of reactive blue 19 dye from aqueous solution, J. Sci. Adv. Mater. Devices 5 (1) (2020) 65–72.
[51] H. Toiserkani, Fabrication and characterization chitosan/functionalized zinc oxide bionanocomposites and study of their antibacterial activity, Compos. Interfaces 23 (3) (2016) 175–189.
[52] V. Makarov, A. Love, O. Sinitsyna, S. Makarova, I. Yaminsky, M. Taliansky, N. Kalinina, "green" nanotechnologies: synthesis of metal nanoparticles using plants, Acta Naturae (англоязычная версия) 6 (1) (2014) 35–44, 20.
[53] R.S. Hamida, M.A. Ali, N. Mugren, M.I. Al-Zaban, M.M. Bin-Meferij, A. Redhwan, Planophila laetevirens-mediated synthesis of silver nanoparticles: optimization, characterization, and anticancer and antibacterial potentials, ACS Omega 8 (32) (2023) 29169–29188.
[54] J.C. Stevens Barrón, C. Chapa González, E. Álvarez Parrilla, L.A. De la Rosa, Nanoparticle-mediated delivery of flavonoids: impact on proinflammatory cytokine production: a systematic review, Biomolecules 13 (7) (2023).
[55] F. Raza, H. Zafar, A. Azad, M. Sulaiman, Factors influencing the green synthesis of metallic nanoparticles using plant extracts: a comprehensive review, Pharmaceutical Fronts 5 (3) (2023) e117–e131.
[56] M.G. Mehrabani, R. Karimian, B. Mehramouz, M. Rahimi, H.S. Kafil, Preparation of biocompatible and biodegradable silk fibroin/chitin/silver nanoparticles 3D scaffolds as a bandage for antimicrobial wound dressing, Int. J. Biol. Macromol. 114 (2018) 961–971.
[57] L. Sukhodub, M. Kumeda, L. Sukhodub, L. Vovchenko, V. Prokopiuk, O. Petrenko, I. Kovalenko, R. Pshenychnyi, A. Opanasyuk, Effect of zinc oxide micro- and nanoparticles on cytotoxicity, antimicrobial activity and mechanical properties of apatite-polymer osteoplastic material, J. Mech. Behav. Biomed. Mater. 150 (2024) 106289.
[58] N. Hassan, T. Krieg, M. Zinser, K. Schröder, N. Kröger, An overview of scaffolds and biomaterials for skin expansion and soft tissue regeneration: insights on zinc and magnesium as new potential key elements, Polymers 15 (19) (2023) 3854.
[59] I. Cavallo, F. Sivori, A. Mastrofrancesco, E. Abril, M. Pontone, E.G. Di Domenico, F. Pimpinelli, Bacterial biofilm in chronic wounds and possible therapeutic approaches, Biology 13 (2) (2024).
[60] J.E. Karbowniczek, D.P. Ura, U. Stachewicz, Nanoparticles distribution and agglomeration analysis in electrospun fiber based composites for desired mechanical performance of poly(3-hydroxybuty-rate-co-3-hydroxyvalerate (PHBV) scaffolds with hydroxyapatite (HA) and titanium dioxide (TiO2) towards medical applications, Compos. B Eng. 241 (2022) 110011.
[61] P.P. Patil, J.V. Meshram, R.A. Bohara, S.G. Nanaware, S.H. Pawar, ZnO nanoparticle-embedded silk fibroin–polyvinyl alcohol composite film: a potential dressing material for infected wounds, New J. Chem. 42 (17) (2018) 14620–14629.
[62] P. Mosallanezhad, H. Nazockdast, Z. Ahmadi, A. Rostami, Fabrication and characterization of polycaprolactone/chitosan nanofibers containing antibacterial agents of curcumin and ZnO nanoparticles for use as wound dressing, Front. Bioeng. Biotechnol. 10 (2022).
[63] R. Rakhshaei, H. Namazi, H. Hamishehkar, H.S. Kafil, R. Salehi, Synthesized Chitosan–Gelatin/znO nanocomposite scaffold with drug delivery properties: higher antibacterial and lower cytotoxicity effects, J. Appl. Polym. Sci. 136 (22) (2019) 47590.
[64] L. Cai, J. Chen, Z. Liu, H. Wang, H. Yang, W. Ding, Magnesium oxide nanoparticles: effective agricultural antibacterial agent against Ralstonia solanacearum, Front. Microbiol. 9 (2018) 790.